Quantitative evaluation of mantle flow traction on overlying tectonic plate: Linear versus power-law mantle rheology

Fengyuan Cui[1], Zhong-Hai Li[1], and Hui-Ying Fu[1]

[1]University of Chinese Academy of Sciences

November 30, 2023

Abstract

The sub-plate mantle flow traction has been considered as a major driving force for plate motion; however, the force acting on the overlying plate is difficult to be well constrained. One reason lies in the variable rheological flow laws of mantle rocks, e.g. linear versus power-law rheology, applied in previous studies. Here, systematic numerical models are conducted to evaluate the mantle flow traction under variable rheological, geometrical and kinematic conditions. The results indicate that mantle flow traction with power-law rheology is much lower than that with linear rheology under the same mantle/plate velocity contrast. In addition, the existence of lithospheric root in the overlying plate enhances the mantle flow traction. In a regime with reasonable parameters, the mantle flow traction with power-law rheology is comparable to the ridge push on the order of 1012 N/m, whereas that with linear rheology is comparable to the slab pull of 1013 N/m.

Quantitative evaluation of mantle flow traction on overlying tectonic plate: Linear versus power-law mantle rheology

Fengyuan Cui, Zhong-Hai Li*, Hui-Ying Fu

Key Laboratory of Computational Geodynamics, College of Earth and Planetary Sciences, University of Chinese Academy of Sciences, Beijing, China

*Corresponding: li.zhonghai@ucas.ac.cn

Key Points:

- The mantle rheological flow law strongly controls the magnitude of mantle flow traction under specific geometric and kinematic conditions.
- The mantle flow traction with power-law rheology is much lower than that with linear rheology when other conditions are similar.
- The existence of continental lithospheric root can enhance the mantle flow traction by increasing both the shear and normal forces.

Abstract

The sub-plate mantle flow traction has been considered as a major driving force for plate motion; however, the force acting on the overlying plate is difficult to be well constrained. One reason lies in the variable rheological flow laws of mantle rocks, e.g. linear versus power-law rheology, applied in previous studies. Here, systematic numerical models are conducted to evaluate the mantle flow traction under variable rheological, geometrical and kinematic conditions. The results indicate that mantle flow traction with power-law rheology is much lower than that with linear rheology under the same mantle/plate velocity contrast. In addition, the existence of lithospheric root in the overlying plate enhances the mantle flow traction. In a regime with reasonable parameters, the mantle flow traction with power-law rheology is comparable to the ridge push on the order of 10^{12} N/m, whereas that with linear rheology is comparable to the slab pull of 10^{13} N/m.

Plain Language Summary

The driving force of plate motion and plate tectonics is a puzzling issue. The subducting slab pull, mid-ocean ridge push and sub-plate mantle flow traction are generally considered as three major forces, with the slab pull as the dominant one. The slab pull and ridge push are dependent on density anomaly and gravity potential, which are relatively easy for quantification. The sub-plate mantle flow traction may play critical roles in cases without slab pull and/or with limited ridge push. The mantle traction is mainly dependent on the mantle/plate velocity contrast and mantle rheology, both of which are not easy to be well constrained. Variable rheological flow laws of mantle rocks, e.g. linear versus power-law rheology, have been applied in previous studies, which may strongly affect the mantle flow traction acting on the overlying plate. Here, systematic numerical models have been conducted to quantify mantle flow traction, which indicate that the traction with power-law rheology is much lower than that with linear rheology under similar conditions. In a regime with reasonable parameters, the traction with power-law rheology is comparable to ridge push on the order of 10^{12} N/m, whereas that with linear rheology is comparable to slab pull of 10^{13} N/m.

1. Introduction

The driving force of plate tectonics is a key issue in geodynamics. It mainly includes the subducting slab pull, mid-ocean ridge (MOR) push, mantle plume forcing, as well as the traction of large-scale mantle flow beneath overlying plate (*Turcotte & Schubert*, 2002). The slab pull, generated by the negative buoyancy of cold subducting slab, is generally considered as the major driving force of plate tectonics, with the magnitude on the order of 10^{13} N/m (*Forsyth & Uyeda*, 1975). The ridge push, induced by the potential energy of elevated MOR, has the magnitude of 10^{12} N/m, i.e. one order lower than slab pull (*Turcotte & Schubert*, 2002). The mantle plume could play a significant role in the weakening of overlying lithosphere (*Baes et al.*, 2020, 2021; *Gerya et al.*, 2015; *van Hinsbergen et al.*, 2021; *Leng & Liu*, 2023); however, its mechanical driving force may be less significant due to the point-wise character and short-time activity.

The mantle flow traction (MFT) is relatively hard to be quantitatively evaluated, due to the difficulties in constraining the mantle flow velocity relative to the overlying plate, as well as the exact viscosity and rheological model of the asthenosphere. However, the MFT may play an important role in plate tectonics, especially in the cases with missing slab pull. For example, the Tethys system experiences multiple Wilson's cycles and is characterized by multiple stages of terrane accretion, slab break-off and subduction transference (initiation), during which the slab pull is lack or absent (*Li et al.*, 2023). The continued moving Tethyan chains, from southern to northern hemisphere, indicate supplementary forces are required and the MFT is a candidate (*Li et al.*, 2023). The effect of MFT on plate motion has been investigated previously. For example, *Alvarez* (2010) and *Cande & Stegman* (2011) have proposed that the MFT may be a potential driving force for the long-living collision along the Himalayan belt, which is further defined as a "mantle conveyor belt" (*Becker & Faccenna*, 2011), with the MFT as high as the typical slab pull (*Li et al.*, 2022; *Lu et al.*, 2015, 2021). Meanwhile, based on the analysis of Pacific plate dynamics, *Stotz et al.* (2018) proposed that the MFT may contribute to at least 50% of the total driving forces of Pacific motion. Similarly, the mantle flow-induced driving force has been mentioned in many global mantle convection models (*Coltice et al.*, 2019; *Faccenna et al.*, 2013; *Ghosh & Holt*, 2012; *Mallard et al.*, 2016).

The question is about the quantitative magnitude of MFT. Can it be as high as, or even higher than, the subducting slab pull? The shear force (F_s) at the base of lithosphere in a simplest model can be expressed as:

$$F_s = \sigma_{xy} \cdot L = \eta \cdot \frac{dV_x}{dy} \cdot L \tag{1}$$

where σ_{xy} is the shear stress at the lithosphere-asthenosphere boundary (LAB), L the horizontal domain of mantle flow, η and V_x the constant viscosity and horizontal velocity of sub-plate mantle, respectively. With some typical parameters of $\eta = 10^{20}$ Pa • s, $\frac{dV_x}{dy} = \frac{2\ \mathrm{cm/yr}}{100\ \mathrm{km}}$, and $L = 3000$ km, the final $F_s \approx 1.9$ TN/m, which is even lower than the normal ridge push. In this simple calculation, large uncertainties lie in the viscosity and velocity gradient of sub-plate mantle flow, both of which are dependent on the mantle rheological model. Two contrasting rheological flow laws have been applied in previous numerical models: one is the equivalent linear rheology based on the comparison with multiple large-scale geophysical observations, e.g. GIA, geoid and so on (*Billen & Gurnis*, 2001; *Mitrovica & Forte*, 2004; *Yang & Gurnis*, 2016), and the other is the power-law rheology based on laboratory experiments (e.g., *Hirth & Kohlstedt*, 2003; *Karato & Wu*, 1993; *Ranalli*, 1995). For the latter, mineral physics-based mantle rheology, the grain size has significant effect, with grain size reduction bringing effective rheological weakening (*Bercovici & Ricard*, 2012; *Foley*, 2018; *Mulyukova & Bercovici*, 2018, 2019). These contrasting rheological models can strongly affect the MFT on the overlying plate; however, the quantitative comparison and evaluation are still lacking.

In this study, systematic numerical models have been conducted to calculate the MFT with both linear and power-law rheological models. In addition, the effects of several factors, including grain size of mantle rocks, mantle/plate velocity contrast, as well as existence and thickness of lithospheric root, have been investigated to provide a more quantitative understanding of the MFT and its role in driving plate motion.

2. Numerical Method

The numerical models are conducted with the code I2VIS (*Gerya*, 2010), with specific algorithms in *Li et al.* (2019) and modifications shown in Supporting Information.

2.1. Mantle rheology

The rheological flow law of mantle rock is applied according to *Hirth & Kohlstedt* (2003):

$$\eta_{diffusion|dislocation} = \frac{1}{2}(A_H)^{-\frac{1}{n}}(\dot{\varepsilon}_{II})^{\frac{1-n}{n}} d^{\frac{p}{n}} \exp\left(\frac{E+PV}{nRT}\right) \quad (2)$$

$$\frac{1}{\eta_{ductile}} = \frac{1}{\eta_{diffusion}} + \frac{1}{\eta_{dislocation}}$$

where A_{H} (pre-exponential factor), n (creep exponent), p (grain size exponent), E (activation energy) and V (activation volume) are rheological parameters following *Hirth & Kohlstedt* (2003) (Table S1). Two different types of mantle rheology are compared in this study, i.e. linear (n = 1) versus power-law (n = 3.5) stress/strain rate ratio, with variable grain size (d) of 2.5 mm, 5 mm and 10 mm, respectively (*Faul & Jackson*, 2005; *Hirth & Kohlstedt*, 2003).

2.2. Model configuration

A 2D large-scale (8000 × 800 km^2) numerical model is configured (Figure S1), with a 10-km-thick sticky air layer, a 90-km-thick lithosphere and a 700-km-thick sub-lithospheric mantle in the reference case (Figure S1a). In another set of model, a thicker lithospheric root is configured in the model domain from x = 3000 to 5000 km, with the lithospheric thickness contrast of ΔH = 0 ~ 200 km (Figure S1b). In both models, permeable condition is applied on the left (influx) and right (outflux) boundaries below the bottom of lithosphere, i.e. y > 100 km in depth. Variable sub-plate mantle flow velocity relative to the stagnant overlying plate is prescribed with ΔV = 1 ~ 10 cm/yr. Contrasting effective viscosity fields are calculated under linear or power-law mantle rheology with the grain size of 5 mm in the reference model (Figure S1), in which the mantle viscosity is consistent to the rheological profiles based on joint geophysical inversions (Figure S2). All the other parameters are shown in Supporting Information.

2.3. Calculation of mantle flow traction

The MFT acting on the overlying plate is mainly composed of two parts: shear force at the LAB and normal force at the vertical walls of lithospheric root. Thus, the MFT (F_{mft}) can be simply calculated with neglecting other minor parts:

$$F_{mft} = \int \sigma_{xy} \cdot dL + \int \sigma_{xx} \cdot dH \tag{3}$$

where σ_{xy} is the shear stress at LAB, L the length of domain for shear traction, σ_{xx} the normal stress at the vertical walls of lithospheric root, and H the depth along lithospheric root. Further on, σ_{xy} and σ_{xx} can be expressed as:

$$\sigma_{xy} = 2 \cdot \eta \cdot \dot{\varepsilon}_{xy} = \eta \cdot \left(\frac{\partial V_x}{\partial y} + \frac{\partial V_y}{\partial x} \right) \tag{4}$$

$$\sigma_{xx} = 2 \cdot \eta \cdot \dot{\varepsilon}_{xx} = 2 \cdot \eta \cdot \frac{\partial V_x}{\partial x} \tag{5}$$

where η is the effective viscosity, $\dot{\varepsilon}_{xy}$ the shear strain rate, $\dot{\varepsilon}_{xx}$ the normal strain rate, V_x and V_y the horizontal and vertical velocities of the mantle relative to overlying plate, respectively.

3. Model Result

3.1. Simple model with flat LAB

Firstly, a simple model is applied with a geometrically homogeneous overlying lithosphere (Figure 1a). Thus, the MFT is dominated by the horizontal shear force at the LAB which is represented roughly by the yellow line in Figure 1a. Dynamically, the LAB is defined as the depth where $\frac{\partial V_x}{\partial y}$ is maximum as indicated in Figures S3a and S3c for the models with linear and power-law rheology, respectively.

In the model with linear mantle rheology, the horizontal velocity gradient along *y*-axis ($\frac{\partial V_x}{\partial y}$) at the LAB increases slightly with higher ΔV (Figure 1b), whereas the vertical velocity gradient along *x*-axis ($\frac{\partial V_y}{\partial x}$) at the LAB is nearly zero (Figure S4a). Meanwhile, the effective viscosity (η) at the LAB remains constant, if neglecting the lateral boundaries of model domain (Figure 1c). Finally, the shear stress (σ_{xy}) acting on the LAB in the central model domain increases from 0.5 MPa to around 2.5 MPa with ΔV = 1 to 5 cm/yr (Figure 1d), indicating a roughly linear correlation between shear stress and mantle/plate velocity contrast.

In the model with power-law mantle rheology, $\frac{\partial V_x}{\partial y}$ at the LAB increases greatly with higher ΔV (Figure 1e), whereas the effective viscosity decreases due to the strain-rate-dependent rheology (Figure 1f). Finally, the shear stress (σ_{xy}) acting on the LAB remains a low value from 0.25 MPa to 0.65 MPa, which is much lower than that with linear rheology (c.f. Figures 1g and 1d). It indicates that the MFT on the overlying plate is limited in the regime with power-law rheology and it cannot be increased significantly by increasing the mantle/plate velocity contrast.

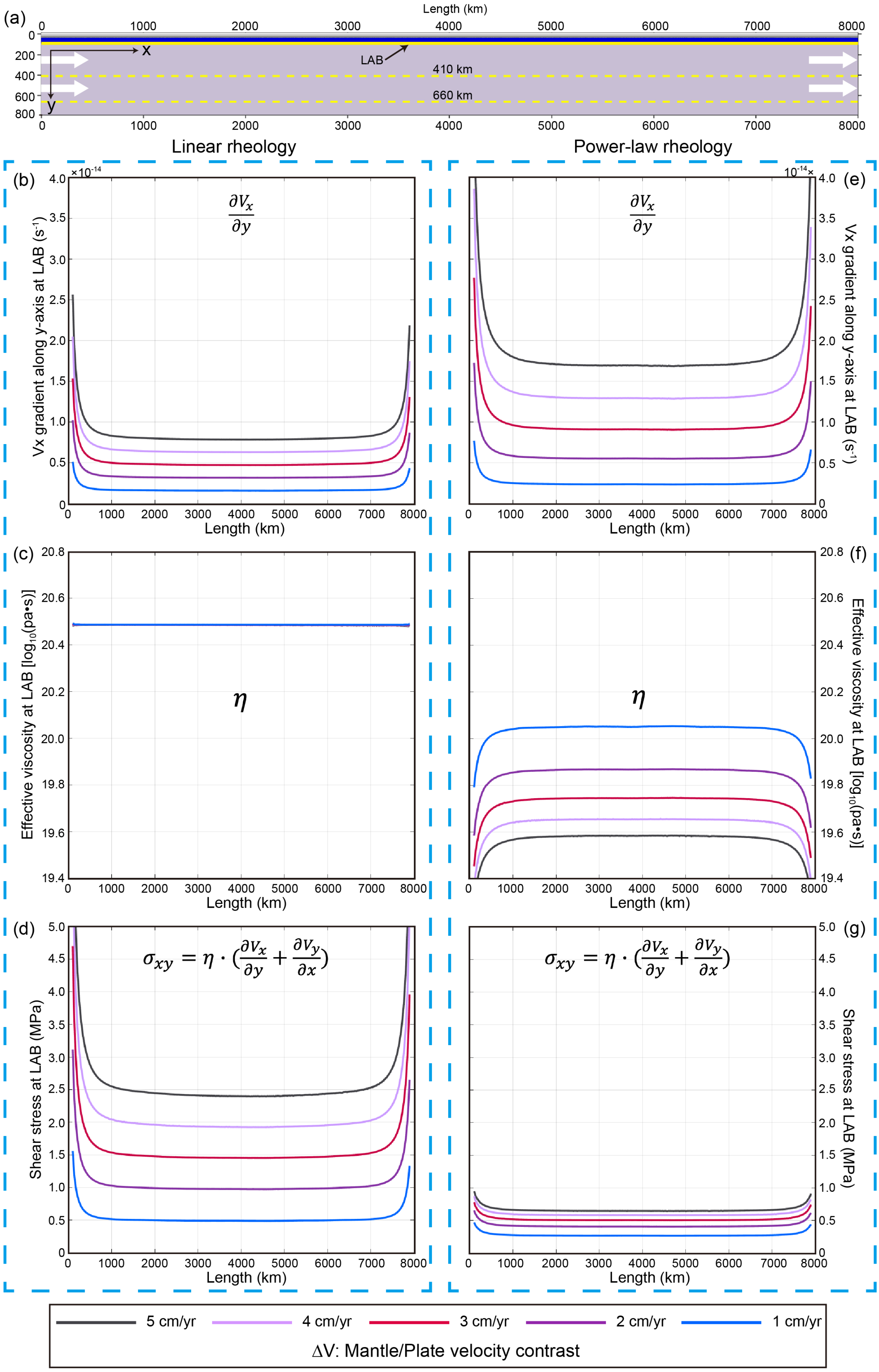

(a)
Length (km)
LAB
410 km
660 km
x
y
Linear rheology
Power-law rheology
(b)
(c)
(d)
(e)
(f)
(g)
$\frac{\partial V_x}{\partial y}$
η
$\sigma_{xy} = \eta \cdot (\frac{\partial V_x}{\partial y} + \frac{\partial V_y}{\partial x})$
Vx gradient along y-axis at LAB (s⁻¹)
Effective viscosity at LAB [log10(pa•s)]
Shear stress at LAB (MPa)
Length (km)
5 cm/yr
4 cm/yr
3 cm/yr
2 cm/yr
1 cm/yr
ΔV: Mantle/Plate velocity contrast

Figure 1. (a) Model configuration. (b-d) The calculated V_x gradient along y-axis ($\frac{\partial V_x}{\partial y}$), effective viscosity ($\eta$) and shear stress ($\sigma_{xy}$) at the LAB with linear rheology, and (e-g) with power-law rheology. Different colors represent different mantle/plate velocity contrasts (ΔV) with colorbar shown at the bottom.

3.2. Model with a lithospheric root

Since the LAB is not always flat, a lithospheric root is applied in this set of models (Figures 2-3). The MFT is composed of both shear force acting on the LAB and normal force acting on the vertical walls of lithospheric root. Dynamically, the vertical walls of lithospheric root are defined as the positions with peak $\frac{\partial V_x}{\partial x}$ values (Figure S3b, d).

Figure 2 shows the calculation of shear stress, which is more complex than that with flat LAB (c.f. Figures 2 and 1), especially in the domain of lithospheric root. However, the general trends are similar. In the models with linear rheology, the shear stress increases greatly (from 0.75 MPa to 3.5 MPa) with increasing ΔV from 1 to 5 cm/yr. In contrast, the power-law rheology results in lower shear stress (from 0.45 MPa to 1 MPa) with the same range of ΔV. Furthermore, the shear stress in the domain of lithospheric root is relatively higher, due to channel-flow-like larger velocity gradient ($\frac{\partial V_x}{\partial y}$). Again, the component of $\frac{\partial V_y}{\partial x}$ has negligible effect on the shear stress (Figure S4c-d).

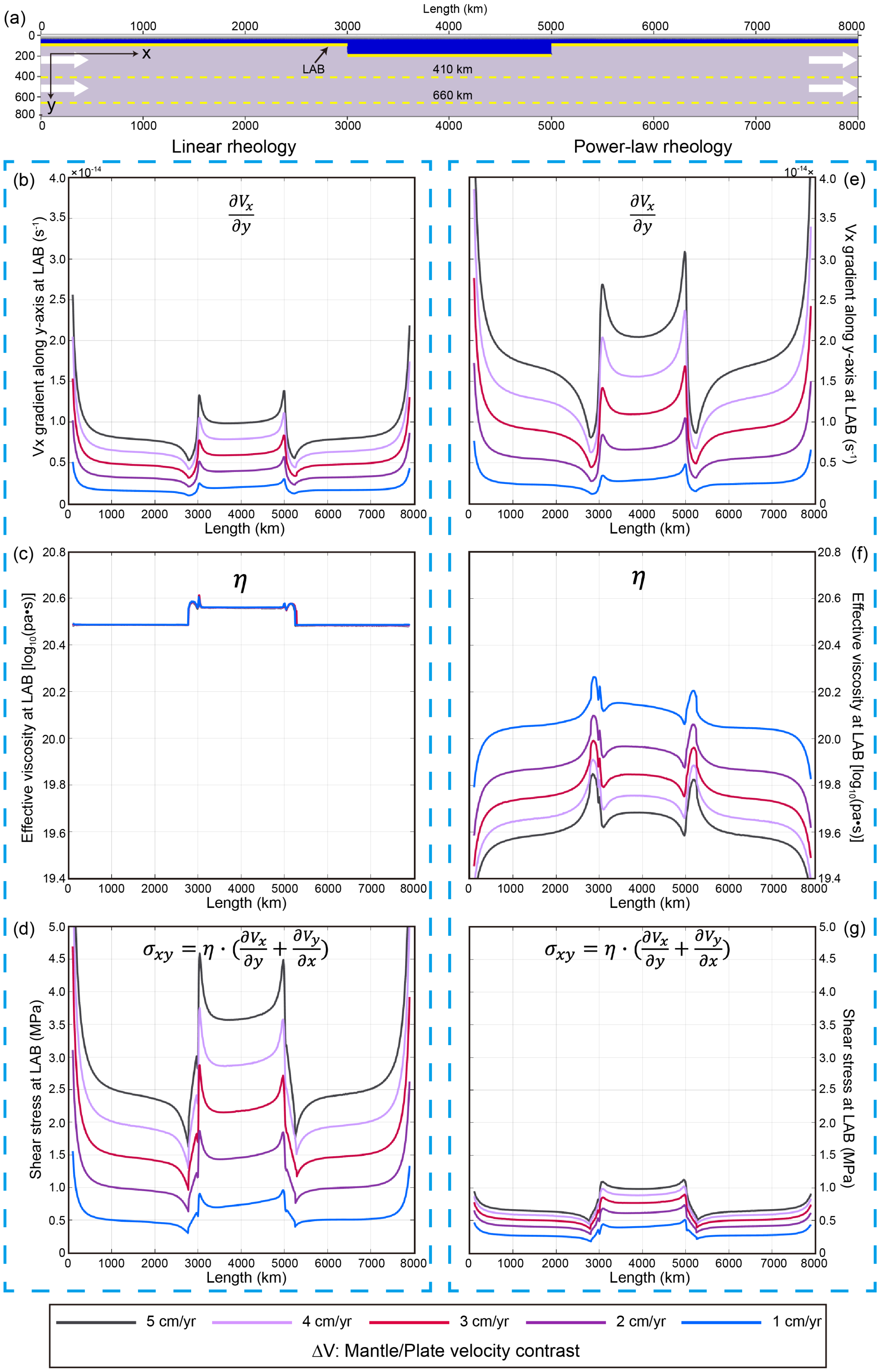

(a)
Length (km)
LAB
410 km
660 km
x
y
Linear rheology
Power-law rheology
(b)
(c)
(d)
(e)
(f)
(g)
Vx gradient along y-axis at LAB (s⁻¹)
Effective viscosity at LAB [log10(pa•s)]
Shear stress at LAB (MPa)
$\frac{\partial V_x}{\partial y}$
η
$\sigma_{xy} = \eta \cdot (\frac{\partial V_x}{\partial y} + \frac{\partial V_y}{\partial x})$
5 cm/yr
4 cm/yr
3 cm/yr
2 cm/yr
1 cm/yr
ΔV: Mantle/Plate velocity contrast

Figure 2. Shear stress calculation in the model with a lithospheric root of ΔH = 100 km (a) Model configuration. (b-d) The calculated V_x gradient along y-axis ($\frac{\partial V_x}{\partial y}$), effective viscosity ($\eta$) and shear stress ($\sigma_{xy}$) at the LAB with linear rheology, and (e-g) with power-law rheology. Different colors represent different mantle/plate velocity contrasts (ΔV) with colorbar shown at the bottom.

The normal stress at the vertical walls of lithospheric root is shown in Figure 3a-c. The normal stress at the left wall is negative, indicating compression, whereas it is positive at the right wall for extension. Thus, both of them contribute to the MFT along the positive x direction. Similar to shear stress, the normal stress with linear rheology is also higher than that with power-law rheology (c.f. Figures 3b and 3c). The detailed calculation routines of normal stress are shown in Figure S5.

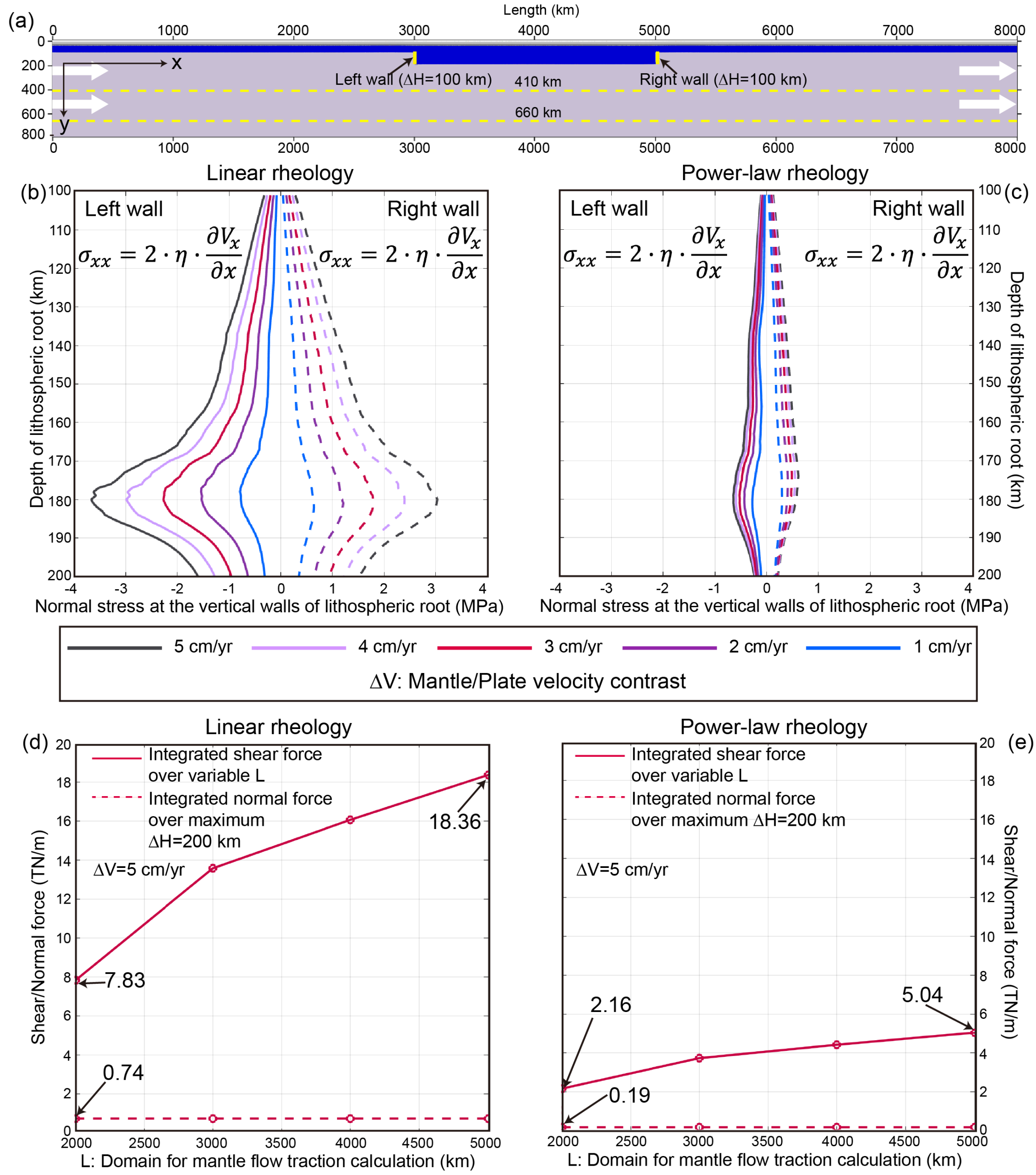

Figure 3. (a-c) Normal stress calculation at the vertical walls of lithospheric root, indicated by the yellow solid lines in (a), with either linear (b) or power-law (c) rheology. The solid and dashed lines represent the normal stress at the left and right walls, respectively. (d-e) Comparison between the integrated shear force (solid red line) over variable domain of MFT (i.e. L in the horizontal axis) and normal force (dashed red line) over a maximum thickness (ΔH = 200 km) of lithospheric root.

The comparison of shear and normal stress indicates that they have similar magnitude in the same model (c.f. Figures 2 and 3); however, the acting domain of them could be quite different. The normal stress acts on the vertical walls of lithosphere root with a maximum ΔH of about 200 km, whereas the shear stress acts on the horizontal LAB which could be thousands of kilometers. As a direct comparison, the shear force with linear rheology ranges from 7.83 to 18.36 TN/m integrating over the length of LAB from 2000 to 5000 km, whereas the normal force is only 0.74 TN/m even with a maximum lithospheric root of ΔH = 200 km. Similarly, the shear force with power-law rheology is also much higher than the normal force. Thus, the normal stress acting on the lithospheric root could be negligible for the large-scale MFT.

3.3. Regime diagrams of mantle flow traction

The above results indicate that the MFT on overlying plate is dependent on multiple factors, including the mantle/plate velocity contrast, thickness of lithospheric root, action domain of mantle flow, as well as the mantle rheology (Figures 1-3). In order to give a systematic evaluation, two regime diagrams with the mantle flow acting domain of 3300 km (i.e. the present-day distance between northern Indian MOR and the Himalaya front) are constructed, with either linear (Figure 4b) or power-law rheology (Figure 4c). Meanwhile, the grain size, as a controlling factor for mantle viscosity, is varied between 2.5 and 10 mm (*Hirth & Kohlstedt, 2003; Karato & Wu, 1995*), with d = 5 mm as the reference value, because it produces viscosity profiles more consistent with geophysical inversions (Figure S2).

The model results indicate that the MFT with linear rheology varies from 0.22 to 62.93 TN/m in the full parameter range of ΔV = 1~10 cm/yr, ΔH = 0~200 km and d = 2.5~10 mm (Figure 4b). In the reference diagram with d = 5 mm, the traction ranges from 1.63 to 29.23 TN/m. In contrast, much lower values are predicted with power-law rheology, i.e. 0.89~5.50 TN/m, in the same range of parameters and d = 5 mm (Figure 4c). Further on, the data in the diagonal of each 2D diagram are plotted in Figure 4d. It shows clearly that the MFT increases with ΔV and ΔH; however, the value with linear rheology could be much higher than the corresponding power-law case. Thus, it is worth noting that when evaluating the MFT, it is better to identify the rheological model first.

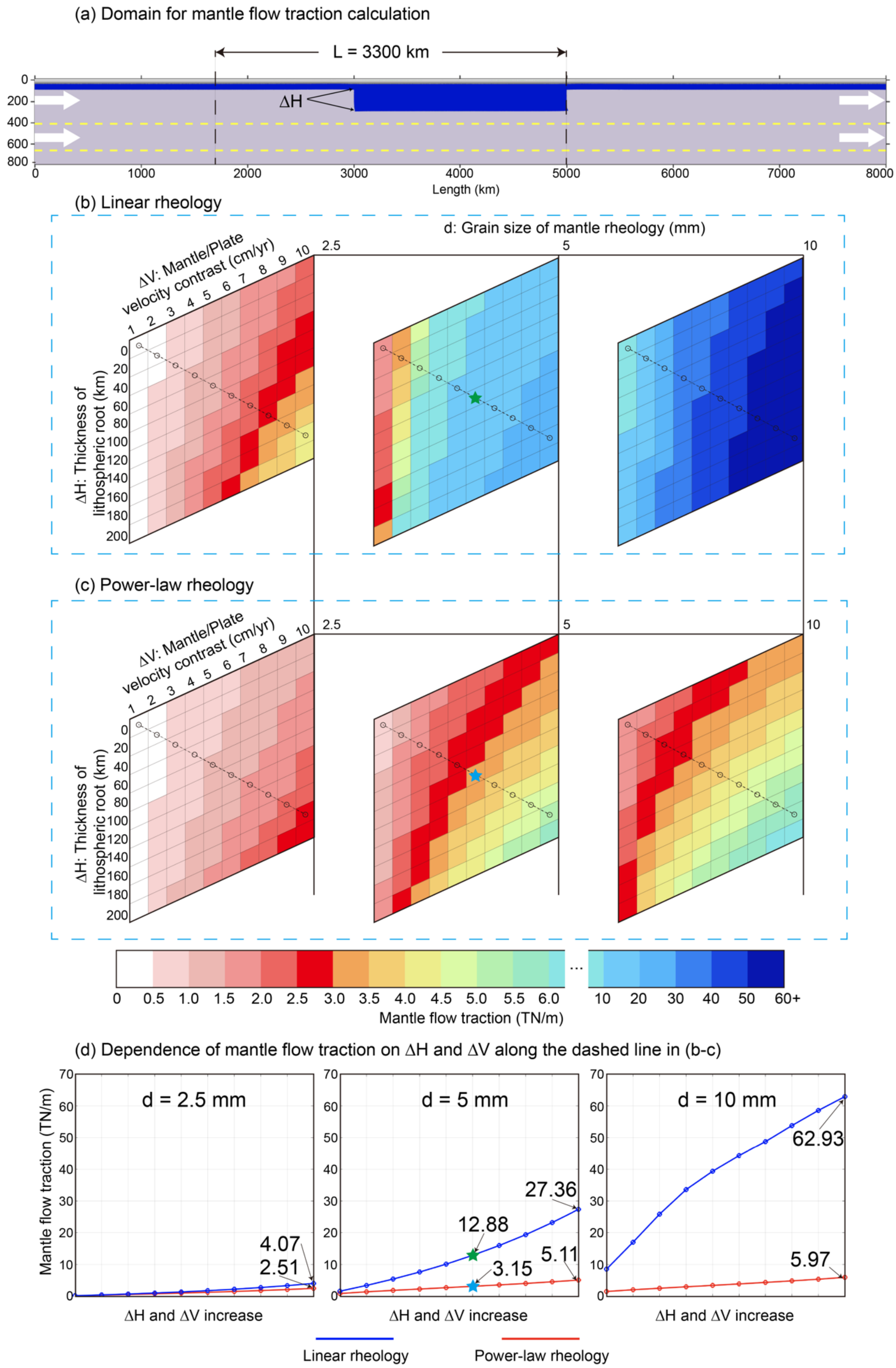

(a) Domain for mantle flow traction calculation
L = 3300 km
ΔH
Length (km)
(b) Linear rheology
d: Grain size of mantle rheology (mm)
ΔV: Mantle/Plate velocity contrast (cm/yr)
ΔH: Thickness of lithospheric root (km)
(c) Power-law rheology
Mantle flow traction (TN/m)
(d) Dependence of mantle flow traction on ΔH and ΔV along the dashed line in (b-c)
d = 2.5 mm
d = 5 mm
d = 10 mm
Mantle flow traction (TN/m)
ΔH and ΔV increase
4.07
2.51
27.36
12.88
5.11
3.15
62.93
5.97
Linear rheology
Power-law rheology

Figure 4. (a) Domain for MFT calculation. (b-c) Phase diagram of MFT with linear and power-law rheology, respectively. The colors represent the value of MFT with the colorbar shown below. (d) Evolution of MFT with increasing thickness of lithospheric root and mantle/plate velocity contrast along the dashed lines in (b-c). The parameters and results of the 660 simulations are shown in Table S3.

4. Discussion

4.1. Effect of linear versus power-law rheology

The systematic numerical models indicate that the MFT with power-law rheology is lower than that with linear rheology in all the comparable cases with variable model configurations and numerical parameters (Figure 4, Table S3). The strain rate-induced weakening at the LAB plays a critical role in reducing the shear traction in the models with power-law rheology (Figures 1-2 and S2). Although the power-law rheology can lead to increase of velocity gradient ($\frac{\partial v_x}{\partial y}$) and thus the high strain rate at the LAB, its effect is much lower than the viscosity drop. Consequently, the latter dominates and results in the drop of MFT in the power-law rheological regime.

The effect of grain size on MFT is more significant in the linear rheological model than the power-law case (Figure 4d), because the grain size can strongly affect the diffusion part of viscous rheology (p = 3 and n = 1 in Equation 2 and Table S1), but does not change the dislocation creep (p = 0 and n = 3.5). Thus, in the regime with a larger grain size and power-law rheology, the dislocation creep dominates and the resulting MFT is limited.

On the other hand, the normal stress at the lateral walls of lithospheric root is also much lower in the power-law than the linear regime (Figures 3 and S5), with a similar mechanism of slightly increased velocity gradient but greatly decreased viscosity. It is worth noting that the walls of lithospheric root are simplified as a vertical boundary in this study, which may be more likely to be inclined. In this latter case, the normal stress may be even smaller.

4.2. Implications for the driving force of Tethyan evolution

The long-term Tethyan evolution experiences multiple Wilson cycles with repeated break-up of continental terranes from Gondwana in the southern hemisphere (Figure 5a), traveling northwards and accreting to Laurasia (Figure 5b). Then the subduction initiation occurs in the neighboring oceanic plate (Figure 5b) and continues the similar process until the final India-Asia collision (Figure 5d). During this evolution, the continental terrane collision and accretion occurs repeatedly with subducting slab break-off. In this situation with slab pull missing, the ridge push and MFT may provide the driving forces for subduction initiation. After a systematic evaluation by numerical models, *Zhong & Li* (2020) suggested that at least 8.5~9 TN/m is required for terrane collision-induced subduction transference (initiation) if no weakness exists in the passive margin. In contrast with lithospheric weakness, the subduction initiation can even occur with only ridge push of ~3 TN/m. In the former case without lithospheric weakness, the residual 5.5-6 TN/m should be provided by other sources. In the present numerical models (Figure 4), the domain for MFT calculation is 3300 km, which is about half the length scale of Paleo-Tethys and Neo-Tethys oceans, i.e. separated by the MOR (*Zhu et al.*, 2021). Based on the results, the MFT can be easily achieved/exceeded with linear rheology, whereas extreme conditions should be satisfied in order to get such a mantle traction in the power-law regime (Figure 4).

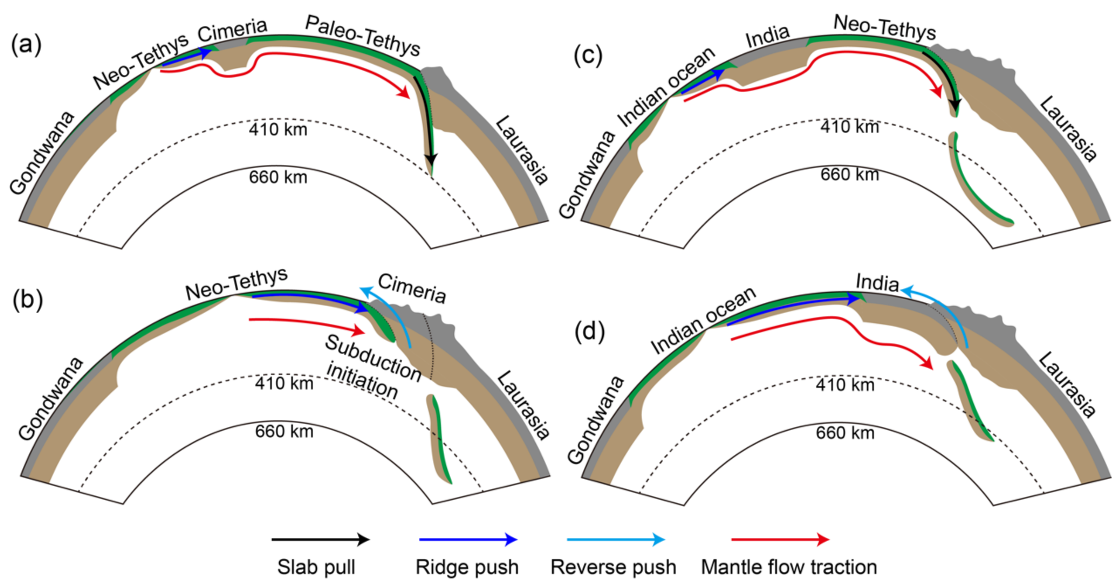

Figure 5. Key stages and possible driving forces of Tethyan evolution. (a) Paleo-Tethys subduction and Neo-Tethys spreading. (b) Collision of Cimerian terrenes with Laurasia and subduction initiation of Neo-Tethys plate. (c) Neo-Tethys subduction and Indian ocean spreading. (d) Continued collision between Indian continent and Laurasia. The arrow lines with different colors represent variable sources of driving forces.

As the final stage of Tethyan evolution, the driving force of India-Asia collision is widely debated. The present Tibetan plateau has an averaged elevation of 5 km, resulting a large push from the gravitation potential energy (GPE) of approximately 6-8 TN/m on the Indian continent and other surround terranes (*Gao et al*., 2022; *Molnar et al*., 1993). Since slab break-off occurs beneath the Tibetan Plateau, the slab pull may be negligible and hard to quantify. Another type of possible force may come from the neighboring Sumatra-Java subduction zone, with its slab pull laterally transmitted to the India-Asia collision zone (*Niu*, 2020). However, the 3D numerical models by *Zhou et al.* (2020) indicate that the lateral transmission of slab pull is dynamically difficult. A full discussion of the above forces can be found in *Li et al.* (2023). In this study, we want to test how the force of Tibetan GPE (6-8 TN/m) can be compensated by the ridge push (3 TN/m) and MFT (3-5 TN/m). The length between northern Indian MOR and Himalayan front is approximately 3300 km, as the case in Figure 4. We reasonably assume the lithospheric thickness contrast between Indian continent and Indian ocean is about 100 km. In order to get a MFT with power-law rheology of 3-5 TN/m, a mantle/plate velocity contrast should be around 6 cm/yr. Although the sub-plate mantle velocity is hard to measure directly, this value is dynamically possible and reasonable. In contrast with a linear rheology, the MFT could be much higher than required.

5. Conclusion

The MFT on overlying plate is systematically and quantitatively evaluated in this study. It indicates that the magnitude of MFT with power-law rheology is much lower than the corresponding linear rheology case. The MFT with linear rheology could be comparable to or even higher than the normal slab pull (>10^{13} N/m), whereas the power-law rheology hinders the significant increase of MFT due to the strain localization and resulting rheological weakening at the LAB depth. In addition, the existence of lithospheric root can enhance the MFT by increasing both the shear and normal stress.

The MFT could facilitate the Tethyan evolution and present-day India-Asia collision. A high mantle flow velocity and existence of lithospheric root are generally required to obtain a reasonable MFT of 3~6 TN/m in the regime with power-law rheology. In contrast, the mantle flow with linear rheology and no strain-rate weakening can easily drive any tectonic movement and deformation; the commonly considered geodynamic difficulties (e.g., subduction initiation at passive margins and long-lasting India-Asia collision) do not exist at all.

Acknowledgments

The research has received funding from the NSFC project (42225403), as well as the Fundamental Research Funds for the Central Universities. Numerical simulations were run with the cluster of National Supercomputer Center in Guangzhou (Tianhe-II) and the GeoModeling Cluster in UCAS.

Open Research

The figures of numerical models are produced by Matlab (https://ww2.mathworks.cn/products/matlab.html) and further compiled by Adobe Illustrator (https://www.adobe.com/cn/products/illustrator.html). The related data are provided in the public repository of Zenodo (https://doi.org/10.5281/zenodo.10184308).

References:

Alvarez, W. (2010). Protracted continental collisions argue for continental plates driven by basal traction. *Earth and Planetary Science Letters*, 296, 434-442. https://doi.org/10.1016/j.epsl.2010.05.030

Baes, M., Sobolv, S., Gerya, T., & Brune, S. (2020). Plume-induced subduction initiation: Single-slab or multi-slab subduction. *Geochemistry, Geophysics, Geosystems*, 21, e2019GC008663. https://doi.org/10.1029/2019GC008663

Baes, M., Sobolev, S., Gerya, T., Stern, R., & Brune, S. (2021). Plate motion and plume-induced subduction initiation. *Gondwana Research*, 98(2021), 277-288. https://doi.org/10.1016/j.gr.2021.06.007

Becker, T. W., & Faccenna, C. (2011). Mantle conveyor beneath the Tethyan collisional belt. Earth and Planetary Science Letters, 310(2011), 453-461. https://doi.org/10.1016/j.epsl.2011.08.021

Bercovici, D., & Ricard, Y. (2012). Mechanisms for the generation of plate tectonics by two-phase grain-damage and pinning. *Physics of the Earth and Planetary Interiors*, 202-203, 27-55. https://doi.org/10.1016/j.pepi.2012.05.003

Billen, M. I., & Gurnis, M. (2001). A low viscosity wedge in subduction zones. *Earth and Planetary Science Letters*, 193(2001), 227-236. https://doi.org/10.1016/S0012-821X(01)00482-4

Cande, S. C., & Stegman, D. R. (2011). Indian and African plate motions driven by the push force of the Reunion plume hear. *Nature*, 475, 47-52. https://doi.org/10.1038/nature10174

Coltice, N., Husson, L., Faccenna, C., & Arnould, M. (2019). What drives tectonic plate? *Science Advances*, 5(10), eaax4295. http://dx.doi.org/10.1126/sciadv.aax4295

Faccenna, C., Becker, T. W., Conrad, C. P., & Husson, L. (2013). Mountain building and mantle dynamics. *Tectonics*, 32(1), 80-93. http://dx.doi.org/10.1029/2012TC003176

Faul, U. H., & Jackson, I. (2005). The seismological signature of temperature and grain size variations in the upper mantle. *Earth and Planetary Science Letters*, 234(2005), 119-134. https://doi.org/10.1016/j.epsl.2005.02.008

Foley, B. J. (2018). The dependence of planetary tectonics on mantle thermal state: applications to early Earth evolution. *Philosophical transactions of the royal society A*, 376: 20170409. https://doi.org/10.1098/rsta.2017.0409

Forsyth, D., & Uyedaf, S. (1975). On the relative importance of the driving forces of plate motion. *Geophysical Journal International*, 43: 163-200. https://doi.org/10.1111/j.1365-246X.1975.tb00631.x

Gao, R., Zhou, H., Guo. X., Lu, Z., Li, W., Wang, H., et al. (2021). Deep seismic reflection evidence on the deep processes of tectonic construction of the Tibetan Plateau. *Earth Science Frontiers*, 28(5): 320-336. https://doi.org/10.13745/j.esf.sf.2021.8.10

Gerya, T. V. (2010). Introduction to numerical geodynamic modelling. Cambridge, UK: Cambridge University Press.

Gerya, T. V., Stern, R. J., Baes, M., Sobolev, S. V., & Whattam, S. A. (2015). Plate tectonics on the Earth triggered by plume-induced subduction initiation. *Nature*, 527, 221-225. https://doi.org/10.1038/nature15752

Ghosh, A., & Holt, W. E. (2012). Plate motions and stresses from global dynamic models. *Science*, 335(6070), 839-843. http://dx.doi.org/10.1126/science.1214209

Hirth, G., & Kohlstedt, D. (2003). Rheology of the upper mantle and the mantle wedge: A view from the experimentalists. *Geophysical Monograph Series*, 138, 83-105. https://doi.org/10.1029/138GM06

Karato, S., & Wu, P. (1993). Rheology of the upper mantle: A synthesis. *Science*, 260(5109), 771-778. https://doi.org/10.1126/science.260.5109.771

Leng, W., & Liu, H. (2023). Progress in the numerical modeling of mantle plumes. *Science China Earth Sciences*, 66(4):685-702. https://doi.org/10.1007/s11430-022-1058-x

Li, Y., Liu, L., Peng, D., 2022. What drives the post-collisional northward Indian motion. *American Geophysical Union Annual Meeting*, DI16A-07

Li, Z.-H., Cui, F., Yang, S., & Zhong, X. Y. (2023). Key geodynamic processes and driving forces of Tethyan evolution. *Science China Earth Sciences*, 66. https://doi.org/10.1007/s11430-022-1083-5

Li, Z.-H., Gerya, T. V., & Connolly, J. A. D. (2019). Variability of subducting slab morphologies in the mantle transition zone: Insight from petrological-thermomechanical modeling. *Earth-Science Reviews*, 196, 102874. https://doi.org/10.1016/j.earscirev.2019.05.018

Lu, G., Kaus, B. J. P., Zhao, L., & Zheng, T. (2015). Self-consistent subduction initiation induced by mantle flow. *Terra Nova*, 27, 130-138. https://doi.org/10.1111/ter.12140

Lu, G., Zhao, L., Chen, L., Wan, B., & Wu, F. Y. (2021). Reviewing subduction initiation and the origin of plate tectonics: What do we learn from present-day Earth? *Earth and Planet Physics*, 5(2), 123-140. http://dx.doi.org/10.26464/epp2021014

Mallard, C., Coltice, N., Seton, M., Muller, R. D., & Tackley, P. J. (2016). Subduction controls the distribution and fragmentation of Earth's tectonic plates. *Nature*, 535(7610), 140-143. http://dx.doi.org/10.1038/nature17992

Mitrovica, J. X., & Forte, A. M. (2004). A new inference of mantle viscosity based upon joint inversion of convection and glacial isostatic adjustment data. *Earth and Planetary Science Letters*, 225(1-2), 177-189. https://doi.org/10.1016/j.epsl.2004.06.005

Molnar, P., England, P., & Martinod, J. (1993). Mantle dynamics, uplift of the Tibetan Plateau, and the Indian Monsoon. *Reviews of Geophysics*, 31: 357-396. https://doi.org/10.1029/93RG02030

Mulyukova, E., & Bercovici, D. (2018). Collapse of passive margins by lithospheric damage and plunging grain size. *Earth and Planetary Science Letters*, 484(2018), 341-352. https://doi.org/10.1016/j.epsl.2017.12.022

Mulyukova, E., & Bercovici, D. (2019). A theoretical model for the evolution of microstructure in lithospheric shear zones. *Geophysical Journal International*, 216, 803-819. https://doi.org/10.1093/gji/ggy467

Niu, Y. (2020). What drives the continued India-Asia convergence since the collision at 55 Ma? *Science Bulletin*, 65(3), 169-172. https://doi.org/10.1016/j.scib.2019.11.018

Ranalli, G. (1995). Rheology of the earth, deformation and flow process in geophysics and geodynamics (2nd ed.). London, UK: Chapman & Hall.

Stotz, I. L., Laffaldano, G., & Davies, D. R. (2018). Pressure-driven poiseuille flow: A major component of the torque-balance governing Pacific plate motion. *Geophysical Research Letters*, 45, 117-125. https://doi.org/10.1002/2017GL075697

Turcotte, D. L., & Schubert, G. (2002). Geodynamics. Cambridge, UK: Cambridge University Press.

van Hinsbergen, D. J. J., Stein, B., Guilmette, C., Maffione, M., Gurer, D., Peters, K., et al. (2021). A record of plume-induced plate rotation triggering subduction initiation. *Nature geoscience*, 14, 626-630. https://doi.org/10.1038/s41561-021-00780-7

Yang, T., & Gurnis, M. (2016). Dynamic topography, gravity and the role of lateral viscosity variations from inversion of global mantle flow. *Geophysical Journal International*, 207(2), 1186-1202. https://doi.org/10.1093/gji/ggw335

Zhong, X. Y., & Li, Z.-H. (2020). Subduction initiation during collision-induced subduction transference: Numerical modelling and implications for the Tethyan evolution. *Journal of Geophysical Research: Solid Earth*, 125(2), e2019JB019288. https://doi.org/10.1029/2019JB019288

Zhou, X., Li, Z.-H., Gerya, T. V., & Stern, R. J. (2020). Lateral propagation-induced subduction initiation at passive continental margins controlled by preexisting lithospheric weakness. Science Advances, 6(10). https://doi.org/10.1126/sciadv.aaz1048

Zhu, R., Zhao, P., & Zhao, L. (2021). Tectonic evolution and geodynamics of the Neo-Tethys Ocean. *Science China Earth Sciences*, 65, 1-24. https://doi.org/10.1007/s11430-021-9845-7

References From the Supporting Information:

Bina, C. R., & Helffrich, G. (1994). Phase transition Clapeyron slopes and transition zone seismic discontinuity topography. *Journal of Geophysical Research*, 99(B8), 15,853–15,860. https://doi.org/10.1029/94JB00462

Bittner, D., & Schmeling, H. (1995). Numerical modeling of melting processes and induced diapirism in the lower crust. *Geophysical Journal International*, 123(1), 59-70. https://doi.org/10.1111/j.1365-246X.1995.tb06661.x

Clauser, C., & Huenges, E. (1995). Thermal conductivity of rocks and minerals. *Rock physics & phase relations*, 105-126. https://doi.org/10.1029/rf003p0105

Dziewonski, A. M., & Anderson, D. L. (1981). Preliminary reference Earth model. *Physics of the Earth and Planetary Interiors*, 25(4), 297–356. https://doi.org/10.1016/0031-9201(81)90046-7

Forte, A. M., Quere, S., Moucha, R., Simmons, N. A., Grand, S. P., Mitrovica, J. X., et al. (2010). Joint seismic-geodynamic-mineral physical modelling of African geodynamics: A reconciliation of deep-mantle convection with surface geophysical constraints. Earth and Planetary Science Letters, 295, 329-341. https://doi.org/10.1016/j.epsl.2010.03.017

Kameyama, M., Yuen, D. A., & Karato, S.-i. (1999). Thermal-mechanical effects of low-temperature plasticity (the Peierls mechanism) on the deformation of a viscoelastic shear zone. *Earth and Planetary Science Letters*, 168(1-2), 159-172. https://doi.org/10.1016/S0012-821X(99)00040-0

Karato, S.-i., Riedel, M. R., & Yuen, D. A. (2001). Rheological structure and deformation of subducted slabs in the mantle transition zone: implications for mantle circulation and deep earthquakes. *Physics of the Earth and Planetary Interiors*, 127(1-4), 83-108. https://doi.org/10.1016/S0031-9201(01)00223-0

Katayama, I., & Karato, S.-i. (2008). Low-temperature, high-stress deformation of olivine under water-saturated conditions. *Physics of the Earth and Planetary Interiors*, 168(3-4), 125-133. https://doi.org/10.1016/j.pepi.2008.05.019

Katz, R. F., Spiegelman, M., & Langmuir, C. H. (2003). A new parameterisation of hydrous mantle melting. *Geochemistry, Geophysics, Geosystems*, 4(9), 1073. https://doi.org/10.1029/2002gc000433

Kirby, K., & Kronenberg, A. K. (1987). Rheology of the lithosphere: Selected topics. *Reviews of Geophysics*, 25(6), 1219-1244. https://doi.org/10.1029/RG025i006p01219

Li, Z.-H., Liu, M., & Gerya, T. (2016). Lithosphere delamination in continental collisional orogens: A systematic numerical study. *Journal of Geophysical Research: Solid Earth*, 121(7), 5186-5211. https://doi.org/10.1002/2016JB013106

Schmidt, M. W., & Poli, S. (1998). Experimentally based water budgets for dehydrating slabs and consequences for arc magma generation. *Earth and Planetary Science Letters*, 163(1-4), 361–379. https://doi.org/10.1016/S0012-821X(98)00142-3

Quantitative evaluation of mantle flow traction on overlying tectonic plate: Linear versus power-law mantle rheology

Fengyuan Cui, Zhong-Hai Li*, Hui-Ying Fu

Key Laboratory of Computational Geodynamics, College of Earth and Planetary Sciences, University of Chinese Academy of Sciences, Beijing, China

*Corresponding: li.zhonghai@ucas.ac.cn

Key Points:

- The mantle rheological flow law strongly controls the magnitude of mantle flow traction under specific geometric and kinematic conditions.
- The mantle flow traction with power-law rheology is much lower than that with linear rheology when other conditions are similar.
- The existence of continental lithospheric root can enhance the mantle flow traction by increasing both the shear and normal forces.

Abstract

The sub-plate mantle flow traction has been considered as a major driving force for plate motion; however, the force acting on the overlying plate is difficult to be well constrained. One reason lies in the variable rheological flow laws of mantle rocks, e.g. linear versus power-law rheology, applied in previous studies. Here, systematic numerical models are conducted to evaluate the mantle flow traction under variable rheological, geometrical and kinematic conditions. The results indicate that mantle flow traction with power-law rheology is much lower than that with linear rheology under the same mantle/plate velocity contrast. In addition, the existence of lithospheric root in the overlying plate enhances the mantle flow traction. In a regime with reasonable parameters, the mantle flow traction with power-law rheology is comparable to the ridge push on the order of 10^{12} N/m, whereas that with linear rheology is comparable to the slab pull of 10^{13} N/m.

Plain Language Summary

The driving force of plate motion and plate tectonics is a puzzling issue. The subducting slab pull, mid-ocean ridge push and sub-plate mantle flow traction are generally considered as three major forces, with the slab pull as the dominant one. The slab pull and ridge push are dependent on density anomaly and gravity potential, which are relatively easy for quantification. The sub-plate mantle flow traction may play critical roles in cases without slab pull and/or with limited ridge push. The mantle traction is mainly dependent on the mantle/plate velocity contrast and mantle rheology, both of which are not easy to be well constrained. Variable rheological flow laws of mantle rocks, e.g. linear versus power-law rheology, have been applied in previous studies, which may strongly affect the mantle flow traction acting on the overlying plate. Here, systematic numerical models have been conducted to quantify mantle flow traction, which indicate that the traction with power-law rheology is much lower than that with linear rheology under similar conditions. In a regime with reasonable parameters, the traction with power-law rheology is comparable to ridge push on the order of 10^{12} N/m, whereas that with linear rheology is comparable to slab pull of 10^{13} N/m.

1. Introduction

The driving force of plate tectonics is a key issue in geodynamics. It mainly includes the subducting slab pull, mid-ocean ridge (MOR) push, mantle plume forcing, as well as the traction of large-scale mantle flow beneath overlying plate (*Turcotte & Schubert*, 2002). The slab pull, generated by the negative buoyancy of cold subducting slab, is generally considered as the major driving force of plate tectonics, with the magnitude on the order of 10^{13} N/m (*Forsyth & Uyeda*, 1975). The ridge push, induced by the potential energy of elevated MOR, has the magnitude of 10^{12} N/m, i.e. one order lower than slab pull (*Turcotte & Schubert*, 2002). The mantle plume could play a significant role in the weakening of overlying lithosphere (*Baes et al.*, 2020, 2021; *Gerya et al.*, 2015; *van Hinsbergen et al.*, 2021; *Leng & Liu*, 2023); however, its mechanical driving force may be less significant due to the point-wise character and short-time activity.

The mantle flow traction (MFT) is relatively hard to be quantitatively evaluated, due to the difficulties in constraining the mantle flow velocity relative to the overlying plate, as well as the exact viscosity and rheological model of the asthenosphere. However, the MFT may play an important role in plate tectonics, especially in the cases with missing slab pull. For example, the Tethys system experiences multiple Wilson's cycles and is characterized by multiple stages of terrane accretion, slab break-off and subduction transference (initiation), during which the slab pull is lack or absent (*Li et al.*, 2023). The continued moving Tethyan chains, from southern to northern hemisphere, indicate supplementary forces are required and the MFT is a candidate (*Li et al.*, 2023). The effect of MFT on plate motion has been investigated previously. For example, *Alvarez* (2010) and *Cande & Stegman* (2011) have proposed that the MFT may be a potential driving force for the long-living collision along the Himalayan belt, which is further defined as a "mantle conveyor belt" (*Becker & Faccenna*, 2011), with the MFT as high as the typical slab pull (*Li et al.*, 2022; *Lu et al.*, 2015, 2021). Meanwhile, based on the analysis of Pacific plate dynamics, *Stotz et al.* (2018) proposed that the MFT may contribute to at least 50% of the total driving forces of Pacific motion. Similarly, the mantle flow-induced driving force has been mentioned in many global mantle convection models (*Coltice et al.*, 2019; *Faccenna et al.*, 2013; *Ghosh & Holt*, 2012; *Mallard et al.*, 2016).

The question is about the quantitative magnitude of MFT. Can it be as high as, or even higher than, the subducting slab pull? The shear force (F_s) at the base of lithosphere in a simplest model can be expressed as:

$$F_s = \sigma_{xy} \cdot L = \eta \cdot \frac{dV_x}{dy} \cdot L \tag{1}$$

where σ_{xy} is the shear stress at the lithosphere-asthenosphere boundary (LAB), L the horizontal domain of mantle flow, η and V_x the constant viscosity and horizontal velocity of sub-plate mantle, respectively. With some typical parameters of $\eta = 10^{20}$ Pa • s, $\frac{dV_x}{dy} = \frac{2\ \mathrm{cm/yr}}{100\ \mathrm{km}}$, and L = 3000 km, the final $F_s \approx$ 1.9 TN/m, which is even lower than the normal ridge push. In this simple calculation, large uncertainties lie in the viscosity and velocity gradient of sub-plate mantle flow, both of which are dependent on the mantle rheological model. Two contrasting rheological flow laws have been applied in previous numerical models: one is the equivalent linear rheology based on the comparison with multiple large-scale geophysical observations, e.g. GIA, geoid and so on (*Billen & Gurnis*, 2001; *Mitrovica & Forte*, 2004; *Yang & Gurnis*, 2016), and the other is the power-law rheology based on laboratory experiments (e.g., *Hirth & Kohlstedt*, 2003; *Karato & Wu*, 1993; *Ranalli*, 1995). For the latter, mineral physics-based mantle rheology, the grain size has significant effect, with grain size reduction bringing effective rheological weakening (*Bercovici & Ricard*, 2012; *Foley*, 2018; *Mulyukova & Bercovici*, 2018, 2019). These contrasting rheological models can strongly affect the MFT on the overlying plate; however, the quantitative comparison and evaluation are still lacking.

In this study, systematic numerical models have been conducted to calculate the MFT with both linear and power-law rheological models. In addition, the effects of several factors, including grain size of mantle rocks, mantle/plate velocity contrast, as well as existence and thickness of lithospheric root, have been investigated to provide a more quantitative understanding of the MFT and its role in driving plate motion.

2. Numerical Method

The numerical models are conducted with the code I2VIS (*Gerya*, 2010), with specific algorithms in *Li et al*. (2019) and modifications shown in Supporting Information.

2.1. Mantle rheology

The rheological flow law of mantle rock is applied according to *Hirth & Kohlstedt* (2003):

$$\eta_{diffusion|dislocation} = \frac{1}{2}(A_H)^{-\frac{1}{n}}(\dot{\varepsilon}_{II})^{\frac{1-n}{n}} d^{\frac{p}{n}} \exp\left(\frac{E+PV}{nRT}\right) \tag{2}$$

$$\frac{1}{\eta_{ductile}} = \frac{1}{\eta_{diffusion}} + \frac{1}{\eta_{dislocation}}$$

where A_{H} (pre-exponential factor), n (creep exponent), p (grain size exponent), E (activation energy) and V (activation volume) are rheological parameters following *Hirth & Kohlstedt* (2003) (Table S1). Two different types of mantle rheology are compared in this study, i.e. linear (n = 1) versus power-law (n = 3.5) stress/strain rate ratio, with variable grain size (d) of 2.5 mm, 5 mm and 10 mm, respectively (*Faul & Jackson*, 2005; *Hirth & Kohlstedt*, 2003).

2.2. Model configuration

A 2D large-scale (8000 × 800 km^2) numerical model is configured (Figure S1), with a 10-km-thick sticky air layer, a 90-km-thick lithosphere and a 700-km-thick sub-lithospheric mantle in the reference case (Figure S1a). In another set of model, a thicker lithospheric root is configured in the model domain from x = 3000 to 5000 km, with the lithospheric thickness contrast of ΔH = 0 ~ 200 km (Figure S1b). In both models, permeable condition is applied on the left (influx) and right (outflux) boundaries below the bottom of lithosphere, i.e. y > 100 km in depth. Variable sub-plate mantle flow velocity relative to the stagnant overlying plate is prescribed with ΔV = 1 ~ 10 cm/yr. Contrasting effective viscosity fields are calculated under linear or power-law mantle rheology with the grain size of 5 mm in the reference model (Figure S1), in which the mantle viscosity is consistent to the rheological profiles based on joint geophysical inversions (Figure S2). All the other parameters are shown in Supporting Information.

2.3. Calculation of mantle flow traction

The MFT acting on the overlying plate is mainly composed of two parts: shear force at the LAB and normal force at the vertical walls of lithospheric root. Thus, the MFT (F_{mft}) can be simply calculated with neglecting other minor parts:

$$F_{mft} = \int \sigma_{xy} \cdot dL + \int \sigma_{xx} \cdot dH \tag{3}$$

where σ_{xy} is the shear stress at LAB, L the length of domain for shear traction, σ_{xx} the normal stress at the vertical walls of lithospheric root, and H the depth along lithospheric root. Further on, σ_{xy} and σ_{xx} can be expressed as:

$$\sigma_{xy} = 2 \cdot \eta \cdot \dot{\varepsilon}_{xy} = \eta \cdot \left(\frac{\partial V_x}{\partial y} + \frac{\partial V_y}{\partial x}\right) \tag{4}$$

$$\sigma_{xx} = 2 \cdot \eta \cdot \dot{\varepsilon}_{xx} = 2 \cdot \eta \cdot \frac{\partial V_x}{\partial x} \tag{5}$$

where η is the effective viscosity, $\dot{\varepsilon}_{xy}$ the shear strain rate, $\dot{\varepsilon}_{xx}$ the normal strain rate, V_x and V_y the horizontal and vertical velocities of the mantle relative to overlying plate, respectively.

3. Model Result

3.1. Simple model with flat LAB

Firstly, a simple model is applied with a geometrically homogeneous overlying lithosphere (Figure 1a). Thus, the MFT is dominated by the horizontal shear force at the LAB which is represented roughly by the yellow line in Figure 1a. Dynamically, the LAB is defined as the depth where $\frac{\partial V_x}{\partial y}$ is maximum as indicated in Figures S3a and S3c for the models with linear and power-law rheology, respectively.

In the model with linear mantle rheology, the horizontal velocity gradient along *y*-axis ($\frac{\partial V_x}{\partial y}$) at the LAB increases slightly with higher ΔV (Figure 1b), whereas the vertical velocity gradient along *x*-axis ($\frac{\partial V_y}{\partial x}$) at the LAB is nearly zero (Figure S4a). Meanwhile, the effective viscosity (η) at the LAB remains constant, if neglecting the lateral boundaries of model domain (Figure 1c). Finally, the shear stress (σ_{xy}) acting on the LAB in the central model domain increases from 0.5 MPa to around 2.5 MPa with ΔV = 1 to 5 cm/yr (Figure 1d), indicating a roughly linear correlation between shear stress and mantle/plate velocity contrast.

In the model with power-law mantle rheology, $\frac{\partial V_x}{\partial y}$ at the LAB increases greatly with higher ΔV (Figure 1e), whereas the effective viscosity decreases due to the strain-rate-dependent rheology (Figure 1f). Finally, the shear stress (σ_{xy}) acting on the LAB remains a low value from 0.25 MPa to 0.65 MPa, which is much lower than that with linear rheology (c.f. Figures 1g and 1d). It indicates that the MFT on the overlying plate is limited in the regime with power-law rheology and it cannot be increased significantly by increasing the mantle/plate velocity contrast.

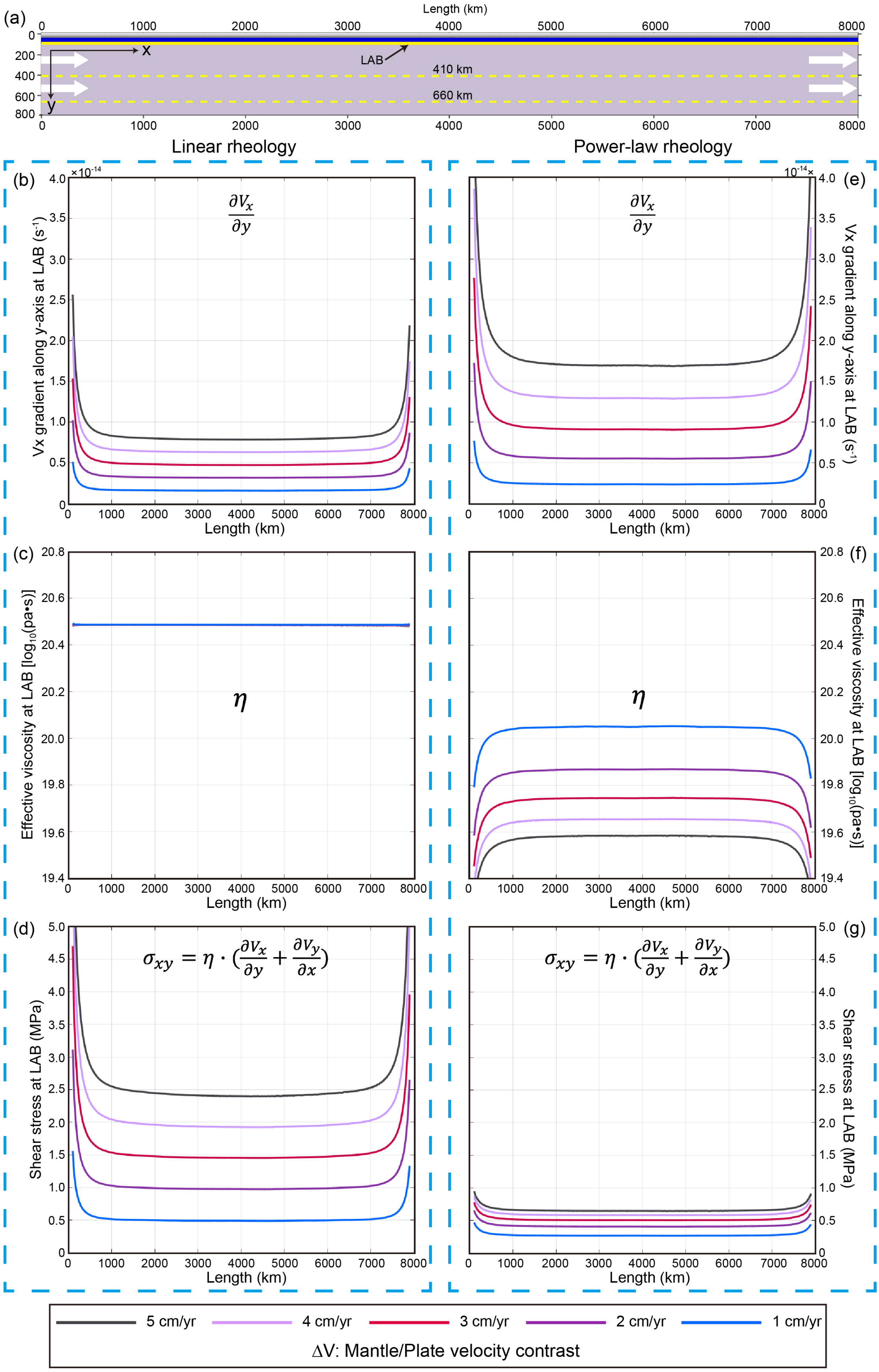

(a)
Length (km)
LAB
410 km
660 km
x
y
Linear rheology
Power-law rheology
(b)
(c)
(d)
(e)
(f)
(g)
Vx gradient along y-axis at LAB (s⁻¹)
Effective viscosity at LAB [log10(pa•s)]
Shear stress at LAB (MPa)
$\frac{\partial V_x}{\partial y}$
η
$\sigma_{xy} = \eta \cdot (\frac{\partial V_x}{\partial y} + \frac{\partial V_y}{\partial x})$
Length (km)
5 cm/yr
4 cm/yr
3 cm/yr
2 cm/yr
1 cm/yr
ΔV: Mantle/Plate velocity contrast

Figure 1. (a) Model configuration. (b-d) The calculated V_x gradient along y-axis ($\frac{\partial V_x}{\partial y}$), effective viscosity ($\eta$) and shear stress ($\sigma_{xy}$) at the LAB with linear rheology, and (e-g) with power-law rheology. Different colors represent different mantle/plate velocity contrasts (ΔV) with colorbar shown at the bottom.

3.2. Model with a lithospheric root

Since the LAB is not always flat, a lithospheric root is applied in this set of models (Figures 2-3). The MFT is composed of both shear force acting on the LAB and normal force acting on the vertical walls of lithospheric root. Dynamically, the vertical walls of lithospheric root are defined as the positions with peak $\frac{\partial V_x}{\partial x}$ values (Figure S3b, d).

Figure 2 shows the calculation of shear stress, which is more complex than that with flat LAB (c.f. Figures 2 and 1), especially in the domain of lithospheric root. However, the general trends are similar. In the models with linear rheology, the shear stress increases greatly (from 0.75 MPa to 3.5 MPa) with increasing ΔV from 1 to 5 cm/yr. In contrast, the power-law rheology results in lower shear stress (from 0.45 MPa to 1 MPa) with the same range of ΔV. Furthermore, the shear stress in the domain of lithospheric root is relatively higher, due to channel-flow-like larger velocity gradient ($\frac{\partial V_x}{\partial y}$). Again, the component of $\frac{\partial V_y}{\partial x}$ has negligible effect on the shear stress (Figure S4c-d).

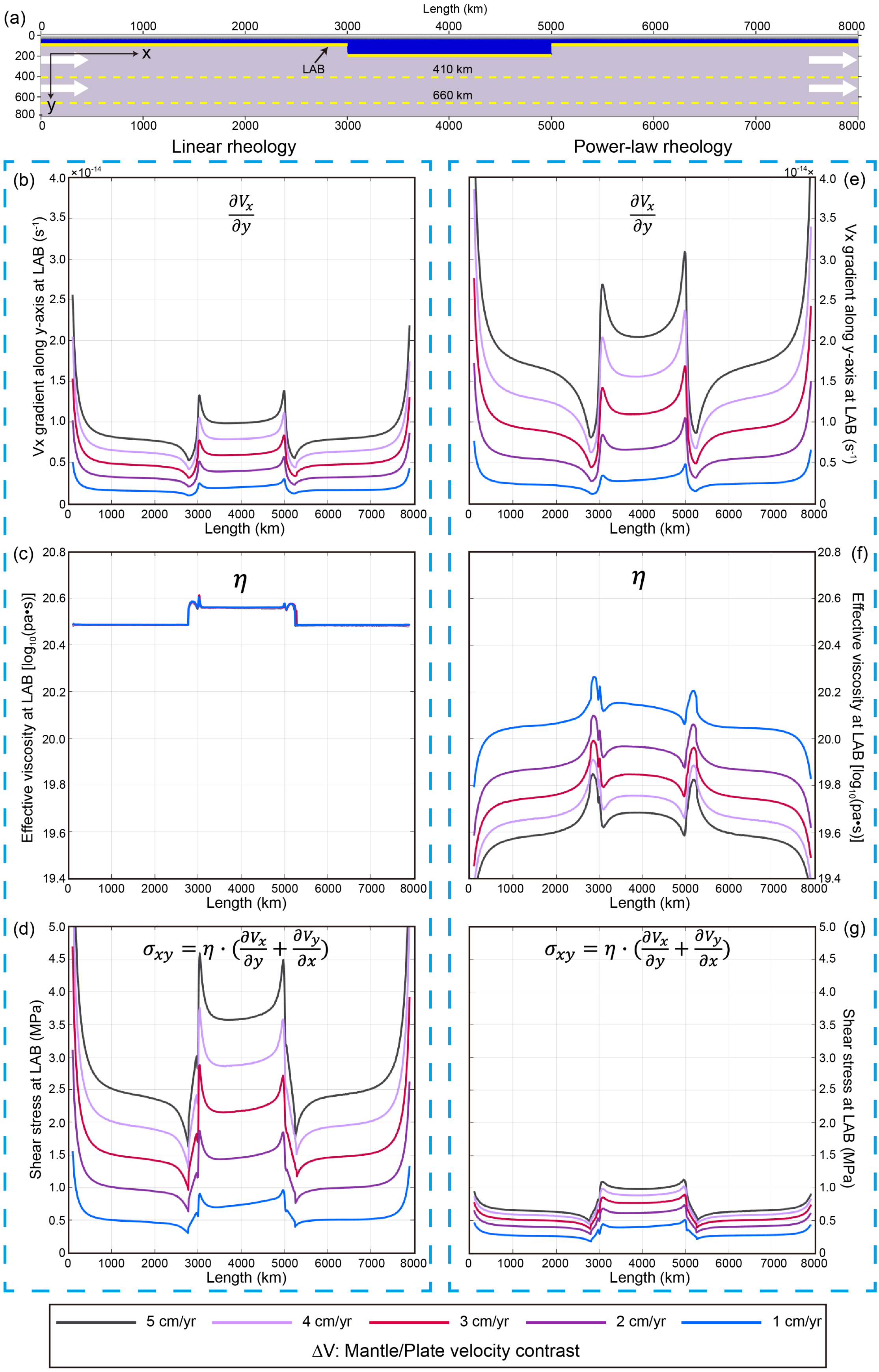

(a)
Length (km)
LAB
x
y
410 km
660 km
Linear rheology
Power-law rheology
(b)
(c)
(d)
(e)
(f)
(g)
$\frac{\partial V_x}{\partial y}$
η
$\sigma_{xy} = \eta \cdot (\frac{\partial V_x}{\partial y} + \frac{\partial V_y}{\partial x})$
Vx gradient along y-axis at LAB (s⁻¹)
Effective viscosity at LAB [log10(pa•s)]
Shear stress at LAB (MPa)
Length (km)
5 cm/yr
4 cm/yr
3 cm/yr
2 cm/yr
1 cm/yr
ΔV: Mantle/Plate velocity contrast

Figure 2. Shear stress calculation in the model with a lithospheric root of ΔH = 100 km (a) Model configuration. (b-d) The calculated V_x gradient along *y*-axis ($\frac{\partial V_x}{\partial y}$), effective viscosity ($\eta$) and shear stress ($\sigma_{xy}$) at the LAB with linear rheology, and (e-g) with power-law rheology. Different colors represent different mantle/plate velocity contrasts (ΔV) with colorbar shown at the bottom.

The normal stress at the vertical walls of lithospheric root is shown in Figure 3a-c. The normal stress at the left wall is negative, indicating compression, whereas it is positive at the right wall for extension. Thus, both of them contribute to the MFT along the positive *x* direction. Similar to shear stress, the normal stress with linear rheology is also higher than that with power-law rheology (c.f. Figures 3b and 3c). The detailed calculation routines of normal stress are shown in Figure S5.

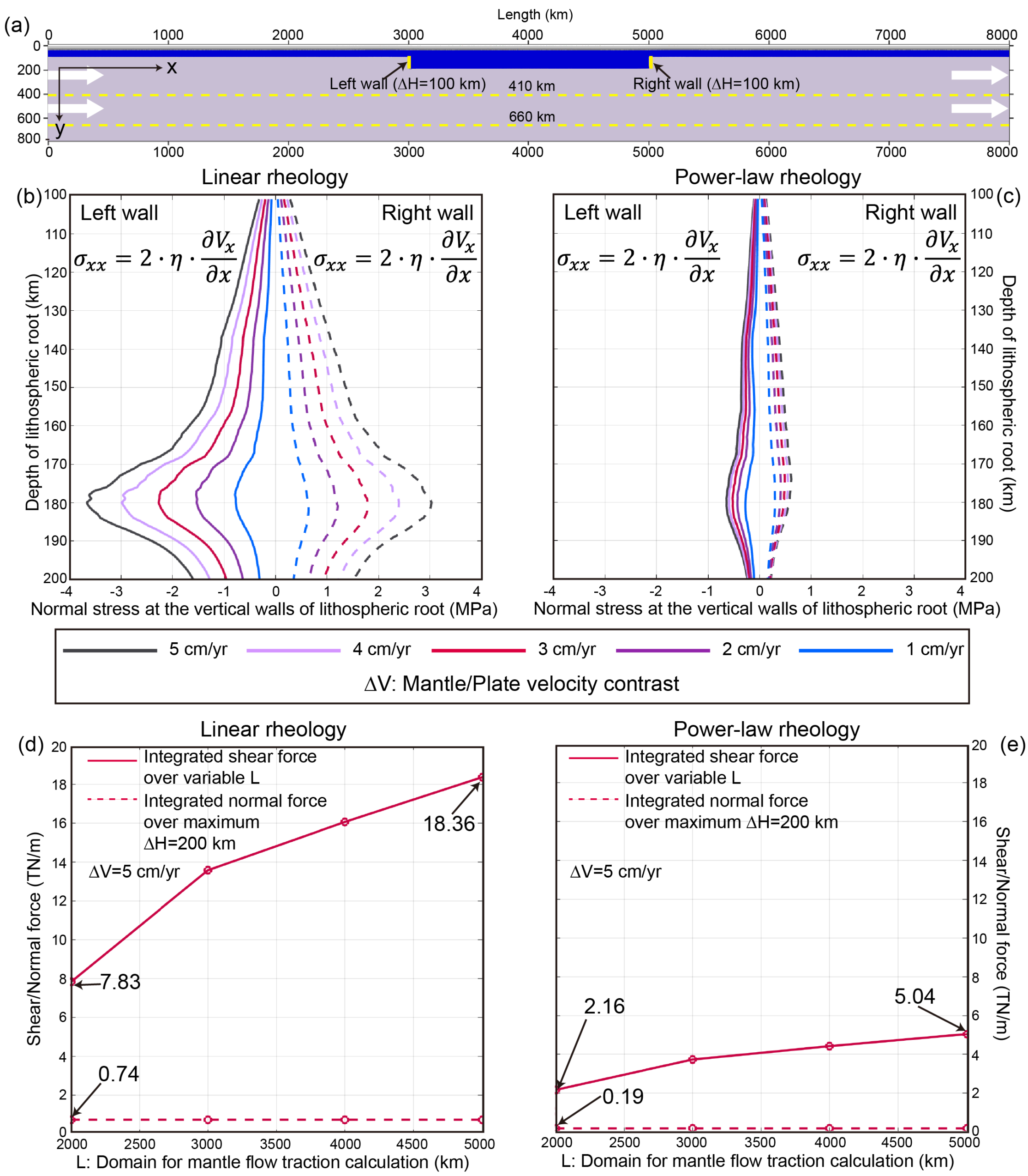

Figure 3. (a-c) Normal stress calculation at the vertical walls of lithospheric root, indicated by the yellow solid lines in (a), with either linear (b) or power-law (c) rheology. The solid and dashed lines represent the normal stress at the left and right walls, respectively. (d-e) Comparison between the integrated shear force (solid red line) over variable domain of MFT (i.e. *L* in the horizontal axis) and normal force (dashed red line) over a maximum thickness (ΔH = 200 km) of lithospheric root.

The comparison of shear and normal stress indicates that they have similar magnitude in the same model (c.f. Figures 2 and 3); however, the acting domain of them could be quite different. The normal stress acts on the vertical walls of lithosphere root with a maximum ΔH of about 200 km, whereas the shear stress acts on the horizontal LAB which could be thousands of kilometers. As a direct comparison, the shear force with linear rheology ranges from 7.83 to 18.36 TN/m integrating over the length of LAB from 2000 to 5000 km, whereas the normal force is only 0.74 TN/m even with a maximum lithospheric root of ΔH = 200 km. Similarly, the shear force with power-law rheology is also much higher than the normal force. Thus, the normal stress acting on the lithospheric root could be negligible for the large-scale MFT.

3.3. Regime diagrams of mantle flow traction

The above results indicate that the MFT on overlying plate is dependent on multiple factors, including the mantle/plate velocity contrast, thickness of lithospheric root, action domain of mantle flow, as well as the mantle rheology (Figures 1-3). In order to give a systematic evaluation, two regime diagrams with the mantle flow acting domain of 3300 km (i.e. the present-day distance between northern Indian MOR and the Himalaya front) are constructed, with either linear (Figure 4b) or power-law rheology (Figure 4c). Meanwhile, the grain size, as a controlling factor for mantle viscosity, is varied between 2.5 and 10 mm (*Hirth & Kohlstedt, 2003; Karato & Wu, 1995*), with d = 5 mm as the reference value, because it produces viscosity profiles more consistent with geophysical inversions (Figure S2).

The model results indicate that the MFT with linear rheology varies from 0.22 to 62.93 TN/m in the full parameter range of ΔV = 1~10 cm/yr, ΔH = 0~200 km and d = 2.5~10 mm (Figure 4b). In the reference diagram with d = 5 mm, the traction ranges from 1.63 to 29.23 TN/m. In contrast, much lower values are predicted with power-law rheology, i.e. 0.89~5.50 TN/m, in the same range of parameters and d = 5 mm (Figure 4c). Further on, the data in the diagonal of each 2D diagram are plotted in Figure 4d. It shows clearly that the MFT increases with ΔV and ΔH; however, the value with linear rheology could be much higher than the corresponding power-law case. Thus, it is worth noting that when evaluating the MFT, it is better to identify the rheological model first.

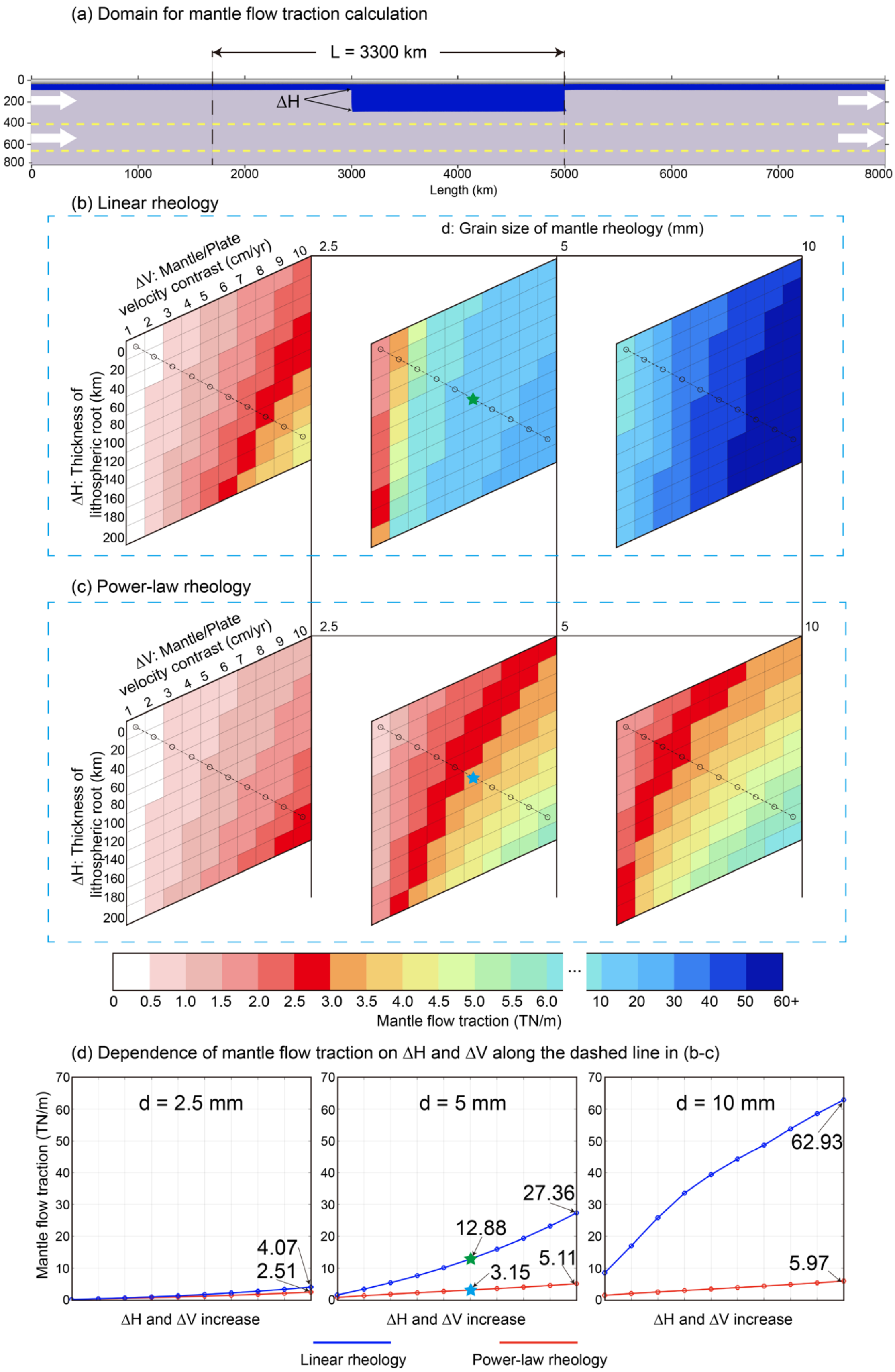
(a) Domain for mantle flow traction calculation
L = 3300 km
ΔH
Length (km)
(b) Linear rheology
d: Grain size of mantle rheology (mm)
ΔV: Mantle/Plate velocity contrast (cm/yr)
ΔH: Thickness of lithospheric root (km)
(c) Power-law rheology
Mantle flow traction (TN/m)
(d) Dependence of mantle flow traction on ΔH and ΔV along the dashed line in (b-c)
Mantle flow traction (TN/m)
d = 2.5 mm
d = 5 mm
d = 10 mm
4.07
2.51
27.36
12.88
5.11
3.15
62.93
5.97
ΔH and ΔV increase
Linear rheology
Power-law rheology

Figure 4. (a) Domain for MFT calculation. (b-c) Phase diagram of MFT with linear and power-law rheology, respectively. The colors represent the value of MFT with the colorbar shown below. (d) Evolution of MFT with increasing thickness of lithospheric root and mantle/plate velocity contrast along the dashed lines in (b-c). The parameters and results of the 660 simulations are shown in Table S3.

4. Discussion

4.1. Effect of linear versus power-law rheology

The systematic numerical models indicate that the MFT with power-law rheology is lower than that with linear rheology in all the comparable cases with variable model configurations and numerical parameters (Figure 4, Table S3). The strain rate-induced weakening at the LAB plays a critical role in reducing the shear traction in the models with power-law rheology (Figures 1-2 and S2). Although the power-law rheology can lead to increase of velocity gradient ($\frac{\partial V_x}{\partial y}$) and thus the high strain rate at the LAB, its effect is much lower than the viscosity drop. Consequently, the latter dominates and results in the drop of MFT in the power-law rheological regime.

The effect of grain size on MFT is more significant in the linear rheological model than the power-law case (Figure 4d), because the grain size can strongly affect the diffusion part of viscous rheology (p = 3 and n = 1 in Equation 2 and Table S1), but does not change the dislocation creep (p = 0 and n = 3.5). Thus, in the regime with a larger grain size and power-law rheology, the dislocation creep dominates and the resulting MFT is limited.

On the other hand, the normal stress at the lateral walls of lithospheric root is also much lower in the power-law than the linear regime (Figures 3 and S5), with a similar mechanism of slightly increased velocity gradient but greatly decreased viscosity. It is worth noting that the walls of lithospheric root are simplified as a vertical boundary in this study, which may be more likely to be inclined. In this latter case, the normal stress may be even smaller.

4.2. Implications for the driving force of Tethyan evolution

The long-term Tethyan evolution experiences multiple Wilson cycles with repeated break-up of continental terranes from Gondwana in the southern hemisphere (Figure 5a), traveling northwards and accreting to Laurasia (Figure 5b). Then the subduction initiation occurs in the neighboring oceanic plate (Figure 5b) and continues the similar process until the final India-Asia collision (Figure 5d). During this evolution, the continental terrane collision and accretion occurs repeatedly with subducting slab break-off. In this situation with slab pull missing, the ridge push and MFT may provide the driving forces for subduction initiation. After a systematic evaluation by numerical models, *Zhong & Li* (2020) suggested that at least 8.5~9 TN/m is required for terrane collision-induced subduction transference (initiation) if no weakness exists in the passive margin. In contrast with lithospheric weakness, the subduction initiation can even occur with only ridge push of ~3 TN/m. In the former case without lithospheric weakness, the residual 5.5-6 TN/m should be provided by other sources. In the present numerical models (Figure 4), the domain for MFT calculation is 3300 km, which is about half the length scale of Paleo-Tethys and Neo-Tethys oceans, i.e. separated by the MOR (*Zhu et al.*, 2021). Based on the results, the MFT can be easily achieved/exceeded with linear rheology, whereas extreme conditions should be satisfied in order to get such a mantle traction in the power-law regime (Figure 4).

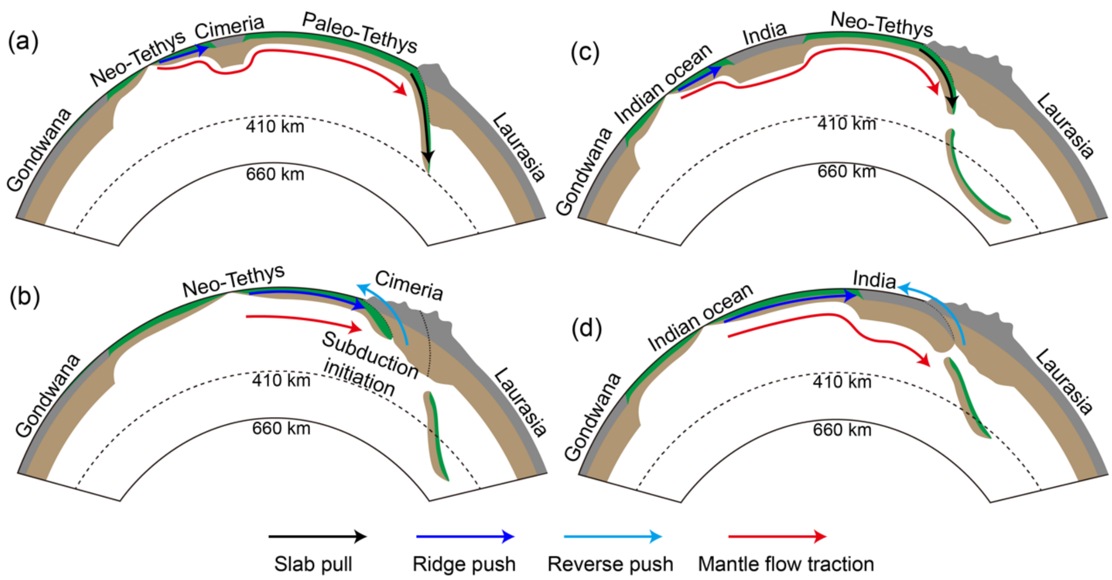

Figure 5. Key stages and possible driving forces of Tethyan evolution. (a) Paleo-Tethys subduction and Neo-Tethys spreading. (b) Collision of Cimerian terrenes with Laurasia and subduction initiation of Neo-Tethys plate. (c) Neo-Tethys subduction and Indian ocean spreading. (d) Continued collision between Indian continent and Laurasia. The arrow lines with different colors represent variable sources of driving forces.

As the final stage of Tethyan evolution, the driving force of India-Asia collision is widely debated. The present Tibetan plateau has an averaged elevation of 5 km, resulting a large push from the gravitation potential energy (GPE) of approximately 6-8 TN/m on the Indian continent and other surround terranes (*Gao et al.*, 2022; *Molnar et al.*, 1993). Since slab break-off occurs beneath the Tibetan Plateau, the slab pull may be negligible and hard to quantify. Another type of possible force may come from the neighboring Sumatra-Java subduction zone, with its slab pull laterally transmitted to the India-Asia collision zone (*Niu*, 2020). However, the 3D numerical models by *Zhou et al.* (2020) indicate that the lateral transmission of slab pull is dynamically difficult. A full discussion of the above forces can be found in *Li et al.* (2023). In this study, we want to test how the force of Tibetan GPE (6-8 TN/m) can be compensated by the ridge push (3 TN/m) and MFT (3-5 TN/m). The length between northern Indian MOR and Himalayan front is approximately 3300 km, as the case in Figure 4. We reasonably assume the lithospheric thickness contrast between Indian continent and Indian ocean is about 100 km. In order to get a MFT with power-law rheology of 3-5 TN/m, a mantle/plate velocity contrast should be around 6 cm/yr. Although the sub-plate mantle velocity is hard to measure directly, this value is dynamically possible and reasonable. In contrast with a linear rheology, the MFT could be much higher than required.

5. Conclusion

The MFT on overlying plate is systematically and quantitatively evaluated in this study. It indicates that the magnitude of MFT with power-law rheology is much lower than the corresponding linear rheology case. The MFT with linear rheology could be comparable to or even higher than the normal slab pull (>10^{13} N/m), whereas the power-law rheology hinders the significant increase of MFT due to the strain localization and resulting rheological weakening at the LAB depth. In addition, the existence of lithospheric root can enhance the MFT by increasing both the shear and normal stress.

The MFT could facilitate the Tethyan evolution and present-day India-Asia collision. A high mantle flow velocity and existence of lithospheric root are generally required to obtain a reasonable MFT of 3~6 TN/m in the regime with power-law rheology. In contrast, the mantle flow with linear rheology and no strain-rate weakening can easily drive any tectonic movement and deformation; the commonly considered geodynamic difficulties (e.g., subduction initiation at passive margins and long-lasting India-Asia collision) do not exist at all.

Acknowledgments

The research has received funding from the NSFC project (42225403), as well as the Fundamental Research Funds for the Central Universities. Numerical simulations were run with the cluster of National Supercomputer Center in Guangzhou (Tianhe-II) and the GeoModeling Cluster in UCAS.

Open Research

The figures of numerical models are produced by Matlab (https://ww2.mathworks.cn/products/matlab.html) and further compiled by Adobe Illustrator (https://www.adobe.com/cn/products/illustrator.html). The related data are provided in the public repository of Zenodo (https://doi.org/10.5281/zenodo.10184308).

References:

Alvarez, W. (2010). Protracted continental collisions argue for continental plates driven by basal traction. *Earth and Planetary Science Letters*, 296, 434-442. https://doi.org/10.1016/j.epsl.2010.05.030

Baes, M., Sobolv, S., Gerya, T., & Brune, S. (2020). Plume-induced subduction initiation: Single-slab or multi-slab subduction. *Geochemistry, Geophysics, Geosystems*, 21, e2019GC008663. https://doi.org/10.1029/2019GC008663

Baes, M., Sobolev, S., Gerya, T., Stern, R., & Brune, S. (2021). Plate motion and plume-induced subduction initiation. *Gondwana Research*, 98(2021), 277-288. https://doi.org/10.1016/j.gr.2021.06.007

Becker, T. W., & Faccenna, C. (2011). Mantle conveyor beneath the Tethyan collisional belt. Earth and Planetary Science Letters, 310(2011), 453-461. https://doi.org/10.1016/j.epsl.2011.08.021

Bercovici, D., & Ricard, Y. (2012). Mechanisms for the generation of plate tectonics by two-phase grain-damage and pinning. *Physics of the Earth and Planetary Interiors*, 202-203, 27-55. https://doi.org/10.1016/j.pepi.2012.05.003

Billen, M. I., & Gurnis, M. (2001). A low viscosity wedge in subduction zones. *Earth and Planetary Science Letters*, 193(2001), 227-236. https://doi.org/10.1016/S0012-821X(01)00482-4

Cande, S. C., & Stegman, D. R. (2011). Indian and African plate motions driven by the push force of the Reunion plume hear. *Nature*, 475, 47-52. https://doi.org/10.1038/nature10174

Coltice, N., Husson, L., Faccenna, C., & Arnould, M. (2019). What drives tectonic plate? *Science Advances*, 5(10), eaax4295. http://dx.doi.org/10.1126/sciadv.aax4295

Faccenna, C., Becker, T. W., Conrad, C. P., & Husson, L. (2013). Mountain building and mantle dynamics. *Tectonics*, 32(1), 80-93. http://dx.doi.org/10.1029/2012TC003176

Faul, U. H., & Jackson, I. (2005). The seismological signature of temperature and grain size variations in the upper mantle. *Earth and Planetary Science Letters*, 234(2005), 119-134. https://doi.org/10.1016/j.epsl.2005.02.008

Foley, B. J. (2018). The dependence of planetary tectonics on mantle thermal state: applications to early Earth evolution. *Philosophical transactions of the royal society A*, 376: 20170409. https://doi.org/10.1098/rsta.2017.0409

Forsyth, D., & Uyedaf, S. (1975). On the relative importance of the driving forces of plate motion. *Geophysical Journal International*, 43: 163-200. https://doi.org/10.1111/j.1365-246X.1975.tb00631.x

Gao, R., Zhou, H., Guo. X., Lu, Z., Li, W., Wang, H., et al. (2021). Deep seismic reflection evidence on the deep processes of tectonic construction of the Tibetan Plateau. *Earth Science Frontiers*, 28(5): 320-336. https://doi.org/10.13745/j.esf.sf.2021.8.10

Gerya, T. V. (2010). Introduction to numerical geodynamic modelling. Cambridge, UK: Cambridge University Press.

Gerya, T. V., Stern, R. J., Baes, M., Sobolev, S. V., & Whattam, S. A. (2015). Plate tectonics on the Earth triggered by plume-induced subduction initiation. *Nature*, 527, 221-225. https://doi.org/10.1038/nature15752

Ghosh, A., & Holt, W. E. (2012). Plate motions and stresses from global dynamic models. *Science*, 335(6070), 839-843. http://dx.doi.org/10.1126/science.1214209

Hirth, G., & Kohlstedt, D. (2003). Rheology of the upper mantle and the mantle wedge: A view from the experimentalists. *Geophysical Monograph Series*, 138, 83-105. https://doi.org/10.1029/138GM06

Karato, S., & Wu, P. (1993). Rheology of the upper mantle: A synthesis. *Science*, 260(5109), 771-778. https://doi.org/10.1126/science.260.5109.771

Leng, W., & Liu, H. (2023). Progress in the numerical modeling of mantle plumes. *Science China Earth Sciences*, 66(4):685-702. https://doi.org/10.1007/s11430-022-1058-x

Li, Y., Liu, L., Peng, D., 2022. What drives the post-collisional northward Indian motion. *American Geophysical Union Annual Meeting*, DI16A-07

Li, Z.-H., Cui, F., Yang, S., & Zhong, X. Y. (2023). Key geodynamic processes and driving forces of Tethyan evolution. *Science China Earth Sciences*, 66. https://doi.org/10.1007/s11430-022-1083-5

Li, Z.-H., Gerya, T. V., & Connolly, J. A. D. (2019). Variability of subducting slab morphologies in the mantle transition zone: Insight from petrological-thermomechanical modeling. *Earth-Science Reviews*, 196, 102874. https://doi.org/10.1016/j.earscirev.2019.05.018

Lu, G., Kaus, B. J. P., Zhao, L., & Zheng, T. (2015). Self-consistent subduction initiation induced by mantle flow. *Terra Nova*, 27, 130-138. https://doi.org/10.1111/ter.12140

Lu, G., Zhao, L., Chen, L., Wan, B., & Wu, F. Y. (2021). Reviewing subduction initiation and the origin of plate tectonics: What do we learn from present-day Earth? *Earth and Planet Physics*, 5(2), 123-140. http://dx.doi.org/10.26464/epp2021014

Mallard, C., Coltice, N., Seton, M., Muller, R. D., & Tackley, P. J. (2016). Subduction controls the distribution and fragmentation of Earth's tectonic plates. *Nature*, 535(7610), 140-143. http://dx.doi.org/10.1038/nature17992

Mitrovica, J. X., & Forte, A. M. (2004). A new inference of mantle viscosity based upon joint inversion of convection and glacial isostatic adjustment data. *Earth and Planetary Science Letters*, 225(1-2), 177-189. https://doi.org/10.1016/j.epsl.2004.06.005

Molnar, P., England, P., & Martinod, J. (1993). Mantle dynamics, uplift of the Tibetan Plateau, and the Indian Monsoon. *Reviews of Geophysics*, 31: 357-396. https://doi.org/10.1029/93RG02030

Mulyukova, E., & Bercovici, D. (2018). Collapse of passive margins by lithospheric damage and plunging grain size. *Earth and Planetary Science Letters*, 484(2018), 341-352. https://doi.org/10.1016/j.epsl.2017.12.022

Mulyukova, E., & Bercovici, D. (2019). A theoretical model for the evolution of microstructure in lithospheric shear zones. *Geophysical Journal International*, 216, 803-819. https://doi.org/10.1093/gji/ggy467

Niu, Y. (2020). What drives the continued India-Asia convergence since the collision at 55 Ma? *Science Bulletin*, 65(3), 169-172. https://doi.org/10.1016/j.scib.2019.11.018

Ranalli, G. (1995). Rheology of the earth, deformation and flow process in geophysics and geodynamics (2nd ed.). London, UK: Chapman & Hall.

Stotz, I. L., Laffaldano, G., & Davies, D. R. (2018). Pressure-driven poiseuille flow: A major component of the torque-balance governing Pacific plate motion. *Geophysical Research Letters*, 45, 117-125. https://doi.org/10.1002/2017GL075697

Turcotte, D. L., & Schubert, G. (2002). Geodynamics. Cambridge, UK: Cambridge University Press.

van Hinsbergen, D. J. J., Stein, B., Guilmette, C., Maffione, M., Gurer, D., Peters, K., et al. (2021). A record of plume-induced plate rotation triggering subduction initiation. *Nature geoscience*, 14, 626-630. https://doi.org/10.1038/s41561-021-00780-7

Yang, T., & Gurnis, M. (2016). Dynamic topography, gravity and the role of lateral viscosity variations from inversion of global mantle flow. *Geophysical Journal International*, 207(2), 1186-1202. https://doi.org/10.1093/gji/ggw335

Zhong, X. Y., & Li, Z.-H. (2020). Subduction initiation during collision-induced subduction transference: Numerical modelling and implications for the Tethyan evolution. *Journal of Geophysical Research: Solid Earth*, 125(2), e2019JB019288. https://doi.org/10.1029/2019JB019288

Zhou, X., Li, Z.-H., Gerya, T. V., & Stern, R. J. (2020). Lateral propagation-induced subduction initiation at passive continental margins controlled by preexisting lithospheric weakness. Science Advances, 6(10). https://doi.org/10.1126/sciadv.aaz1048

Zhu, R., Zhao, P., & Zhao, L. (2021). Tectonic evolution and geodynamics of the Neo-Tethys Ocean. *Science China Earth Sciences*, 65, 1-24. https://doi.org/10.1007/s11430-021-9845-7

References From the Supporting Information:

Bina, C. R., & Helffrich, G. (1994). Phase transition Clapeyron slopes and transition zone seismic discontinuity topography. *Journal of Geophysical Research*, 99(B8), 15,853–15,860. https://doi.org/10.1029/94JB00462

Bittner, D., & Schmeling, H. (1995). Numerical modeling of melting processes and induced diapirism in the lower crust. *Geophysical Journal International*, 123(1), 59-70. https://doi.org/10.1111/j.1365-246X.1995.tb06661.x

Clauser, C., & Huenges, E. (1995). Thermal conductivity of rocks and minerals. *Rock physics & phase relations*, 105-126. https://doi.org/10.1029/rf003p0105

Dziewonski, A. M., & Anderson, D. L. (1981). Preliminary reference Earth model. *Physics of the Earth and Planetary Interiors*, 25(4), 297–356. https://doi.org/10.1016/0031-9201(81)90046-7

Forte, A. M., Quere, S., Moucha, R., Simmons, N. A., Grand, S. P., Mitrovica, J. X., et al. (2010). Joint seismic-geodynamic-mineral physical modelling of African geodynamics: A reconciliation of deep-mantle convection with surface geophysical constraints. Earth and Planetary Science Letters, 295, 329-341. https://doi.org/10.1016/j.epsl.2010.03.017

Kameyama, M., Yuen, D. A., & Karato, S.-i. (1999). Thermal-mechanical effects of low-temperature plasticity (the Peierls mechanism) on the deformation of a viscoelastic shear zone. *Earth and Planetary Science Letters*, 168(1-2), 159-172. https://doi.org/10.1016/S0012-821X(99)00040-0

Karato, S.-i., Riedel, M. R., & Yuen, D. A. (2001). Rheological structure and deformation of subducted slabs in the mantle transition zone: implications for mantle circulation and deep earthquakes. *Physics of the Earth and Planetary Interiors*, 127(1-4), 83-108. https://doi.org/10.1016/S0031-9201(01)00223-0

Katayama, I., & Karato, S.-i. (2008). Low-temperature, high-stress deformation of olivine under water-saturated conditions. *Physics of the Earth and Planetary Interiors*, 168(3-4), 125-133. https://doi.org/10.1016/j.pepi.2008.05.019

Katz, R. F., Spiegelman, M., & Langmuir, C. H. (2003). A new parameterisation of hydrous mantle melting. *Geochemistry, Geophysics, Geosystems*, 4(9), 1073. https://doi.org/10.1029/2002gc000433

Kirby, K., & Kronenberg, A. K. (1987). Rheology of the lithosphere: Selected topics. *Reviews of Geophysics*, 25(6), 1219-1244. https://doi.org/10.1029/RG025i006p01219

Li, Z.-H., Liu, M., & Gerya, T. (2016). Lithosphere delamination in continental collisional orogens: A systematic numerical study. *Journal of Geophysical Research: Solid Earth*, 121(7), 5186-5211. https://doi.org/10.1002/2016JB013106

Schmidt, M. W., & Poli, S. (1998). Experimentally based water budgets for dehydrating slabs and consequences for arc magma generation. *Earth and Planetary Science Letters*, 163(1-4), 361–379. https://doi.org/10.1016/S0012-821X(98)00142-3

AGU PUBLICATIONS

Geophysical Research Letters

Supporting Information for

Quantitative evaluation of mantle flow traction on overlying tectonic plate: Linear versus power-law mantle rheology

Fengyuan Cui, Zhong-Hai Li*, Hui-Ying Fu

Key Laboratory of Computational Geodynamics, College of Earth and Planetary Sciences, University of Chinese Academy of Sciences, Beijing, China

*Corresponding: <li.zhonghai@ucas.ac.cn>

Contents of this file

Text S1 to S2

Figures S1 to S5

Tables S1 to S3

Text S1. The numerical methods

The numerical models are conducted with the finite difference code I2VIS, which combines fixed Eulerian nodal points and movable Lagrangian markers, and please refer to Gerya (2010) and Li et al. (2019) for details.

1 Governing equations

Three sets of conservation equations (mass, momentum and energy) as well as the constitutive relationships are solved in numerical models (Gerya, 2010).

(1) Stokes equation:

$$\frac{\partial \sigma'_{ij}}{\partial x_j} = \frac{\partial P}{\partial x_i} - \rho(C, M, P, T) g_i \quad (i, j = 1,2)$$

Where σ' is the deviatoric stress tensor, x the spatial coordinate, and g the gravitational acceleration. ρ is the density which depends on composition (C), melt fraction (M), dynamic pressure (P) and temperature (T). The density for a specific rock type can be described as:

$$\rho = \rho_{solid} - M(\rho_{solid} - \rho_{molten})$$

$$\rho_{solid|molten} = \rho_0[1 - \alpha(T - T_0)][1 + \beta(P - P_0)]$$

Where ρ_0 is the density in the reference condition with P_0= 0.1 MPa and $T_0 =$ 298 K. α and β are the thermal expansion coefficient and the compressibility coefficient, respectively, as shown in Table S2. Rock density is further adjusted for phase transitions.

The constitutive relationship:

$$\sigma'_{ij} = 2\eta_{eff}\dot{\varepsilon}_{ij}$$

$$\dot{\varepsilon}_{ij} = \frac{1}{2}\left(\frac{\partial v_i}{\partial x_j} + \frac{\partial v_j}{\partial x_i}\right)$$

Where $\dot{\varepsilon}$ is the deviatoric strain rate tensor, v the velocity tensor, and η_{eff} the effective viscosity.

(2) Conservation of mass:

The conservation of mass is still approximated by the incompressible continuity equation in the numerical models:

$$\frac{\partial v_i}{\partial x_i} = 0$$

(3) Energy equation:

$$\rho C_p\left(\frac{DT}{Dt}\right) = -\frac{\partial q_i}{\partial x_i} + H$$

$$q_i = -k(C,P,T)\frac{\partial T}{\partial x_i}$$

Where C_p is the effective isobaric heat capacity, DT/Dt the substantive time derivative of temperature, and q the thermal heat flux. H is the heat generation, which includes radioactive heat production (H_r), adiabatic heating (H_a) and shear heating (H_s). k is the thermal conductivity, depending on composition (C), pressure (P) and temperature (T).

2 Visco-Plastic-Peierls rheology

The constitutive relationships are described by the combined visco-plastic-Peierls flow laws. The ductile viscosity ($\eta_{ductile}$), the plastic equivalent ($\eta_{plastic}$) and the Peierls viscosity ($\eta_{peierls}$) of different rock types are calculated separately in numerical models.

(1) Viscous flow law of crustal rocks

The viscosity of continental crust is calculated by the flow law of Ranalli (1995):

$$\eta_{ductile} = \frac{1}{2}(A_R)^{-\frac{1}{n}}(\dot{\varepsilon}_{II})^{\frac{1-n}{n}} exp\left(\frac{E+PV}{nRT}\right)$$

Where $\dot{\varepsilon}_{II}$ is the second invariant of the strain rate tensor, A_R the pre-exponential factor, n the creep exponent, E the activation energy, V the activation volume, and R the gas constant. The flow law parameters are determined by experiments and shown in the Table S1 (Kirby & Kronenberg, 1987; Ranalli, 1995).

(2) Viscous flow law of mantle rocks

For mantle rocks, the viscosity is defined according to Hirth and Kohlstedt (2003):

$$\eta_{diffusion|dislocation} = \frac{1}{2}(A_H)^{-\frac{1}{n}}(\dot{\varepsilon}_{II})^{\frac{1-n}{n}} d^{\frac{p}{n}} exp\left(\frac{E+PV}{nRT}\right)$$

$$\frac{1}{\eta_{ductile}} = \frac{1}{\eta_{diffusion}} + \frac{1}{\eta_{dislocation}}$$

Where A_H (pre-exponential factor), n (creep exponent), p (grain size exponent), r (water content exponent), α (pre-melt-fraction factor), E (activation energy) and V (activation volume) are flow law parameters determined from the laboratory experiments (Table S1). *d* is the grain size (varied from 2.5 mm to 10 mm, and 5 mm in reference models), and *p* the exponent for grain size.

(3) Plastic deformation

The extended Drucker-Prager yield criterion is applied as follows:

$$\eta_{plastic} = \frac{\sigma_{yield}}{2\dot{\varepsilon}_{II}}$$

$$\sigma_{yield} = C_0 + Psin(\varphi_{eff})$$

Where σ_{yield} is the yield stress, C_0 the residual rock strength at P = 0 and P is the dynamic pressure. φ_{eff} is the effective internal friction angle, which includes the possible fluid/melt effects that control the brittle strength of fluid/melt containing porous or fractured media (Li et al., 2016, 2019).

(4) Peierls deformation

The Peierls mechanism is implemented to the deformation by low-temperature and high-pressure plasticity (Kameyama et al., 1999; Karato et al., 2001; Katayama & Karato, 2008):

$$\eta_{peierls} = \frac{1}{2A_{peierls}\sigma_{II}} exp\left(\frac{E+PV}{RT}\left(1-\left(\frac{\sigma_{II}}{\sigma_{peierls}}\right)^p\right)^q\right)$$

Where $A_{peierls}$, p, q, r are experimentally derived material constants. σ_{II} is the second invariant of stress tensor, $\sigma_{peierls}$ a stress value that limits the strength of the material.

(5) Effective viscosity

The effective viscosity is the minimum value among the ductile viscosity ($\eta_{ductile}$), the plastic equivalent ($\eta_{plastic}$), and the Peierls viscosity ($\eta_{peierls}$):

$$\eta_{eff} = \min\left(\eta_{ductile}, \eta_{plastic}, \eta_{peierls}\right)$$

The final viscosity is controlled by the cut-off values of $[10^{18}, 10^{25}]Pa \cdot s$.

3 Phase transitions

The phase transitions at 410 km and 660 km discontinuities are included in the numerical models (e.g., Bina & Helffrich, 1994; Li et al., 2019), which modify the mantle density structure in addition to the gradual pressure and temperature dependence. In the current study, these phase transitions only affect the density, whereas the related variations of latent heat and possible viscosity change are not considered (Li et al., 2019). The resulting density structure of the mantle is consistent with the Preliminary Reference Earth Model (PREM) (Dziewonski & Anderson, 1981). The Clapeyron slopes of 2.0 MPa/K and -1.0 MPa/K are applied for the 410 km and 660 km discontinuities, respectively, which do not affect the model results significantly.

Text S2. Numerical model configuration

The numerical models are configured in a 2-D spatial domain of 8000 km in length and 800 km in depth, as shown in Figure S1a. The spatial resolution of the model is 10 km in the horizontal direction, while that in the vertical direction is 1 km from 0 to 300 km and gradually changes to 10 km downward to the bottom. A 10-km-thick "sticky" air layer with a low density and viscosity is set above the continental lithosphere. The model without lithospheric root contains a 90-km-thick continental lithosphere, including an upper crust of 20 km and a lower crust of 15 km. In contrast, the model with a lithospheric root contains a 2000-km-length thicker lithosphere as shown in Figure S1b. The thickness of lithospheric root is varied, with a value of 100 km in the reference model (i.e. the total lithospheric thickness of 190 km).

For the temperature field configuration, the top and bottom boundaries of the model are set to be 273 K and 1923 K respectively. The initial thermal gradient of the sublithospheric mantle is 0.5 K/km. The initial temperature of the 90-km-thick continental lithosphere-asthenosphere-boundary is 1573 K, with a linear gradient within the lithosphere. The "sticky air" layer remains the constant temperature of 273 K. The left and right boundaries of the model are adiabatic with no horizontal heat flux.

For the mechanical boundary condition, permeable condition is applied below 100 km on the left and right boundaries. Once markers migrate into the model domain across the left boundary, additional markers will migrate out from the right side permeable boundary to guarantee the mass conservation. The prescribed mantle/plate velocity contrast is obtained by setting the markers velocity on permeable boundaries, which is 1 cm/yr in the reference model, as shown by the white arrows in Figure S1a-b. Other boundaries are all free-slip.

For the rheology configuration, all models are conducted with two different rheological models: linear rheology versus power-law rheology. For linear rheology, n (creep exponent as in Equation 2) in the dislocation creep of olivine is set to be 1, which is 3.5 for power-law rheology (Hirth & Kohlstedt, 2003). The viscous flow law of mantle rock is independent of strain rate in the linear rheology regime, whereas the viscosity decreases with strain rate in the power-law rheology regime, as shown in Figure S1c-f.

For the grain size of mantle rheology, it is not well constrained according to the previous studies (e.g., Karato et al., 1995; Hirth & Kohlstedt, 2003). Consequently, three different values are tested and compared: 2.5 mm, 5 mm (reference models) and 10 mm. The simulated effective viscosity profiles with different grain sizes are shown in Figure S2. The profile with grain size of 5 mm is quite consistent with the joint inversions of GIA and global convection observations (Figures S2a and S2d), which is thus chosen as the reference case.

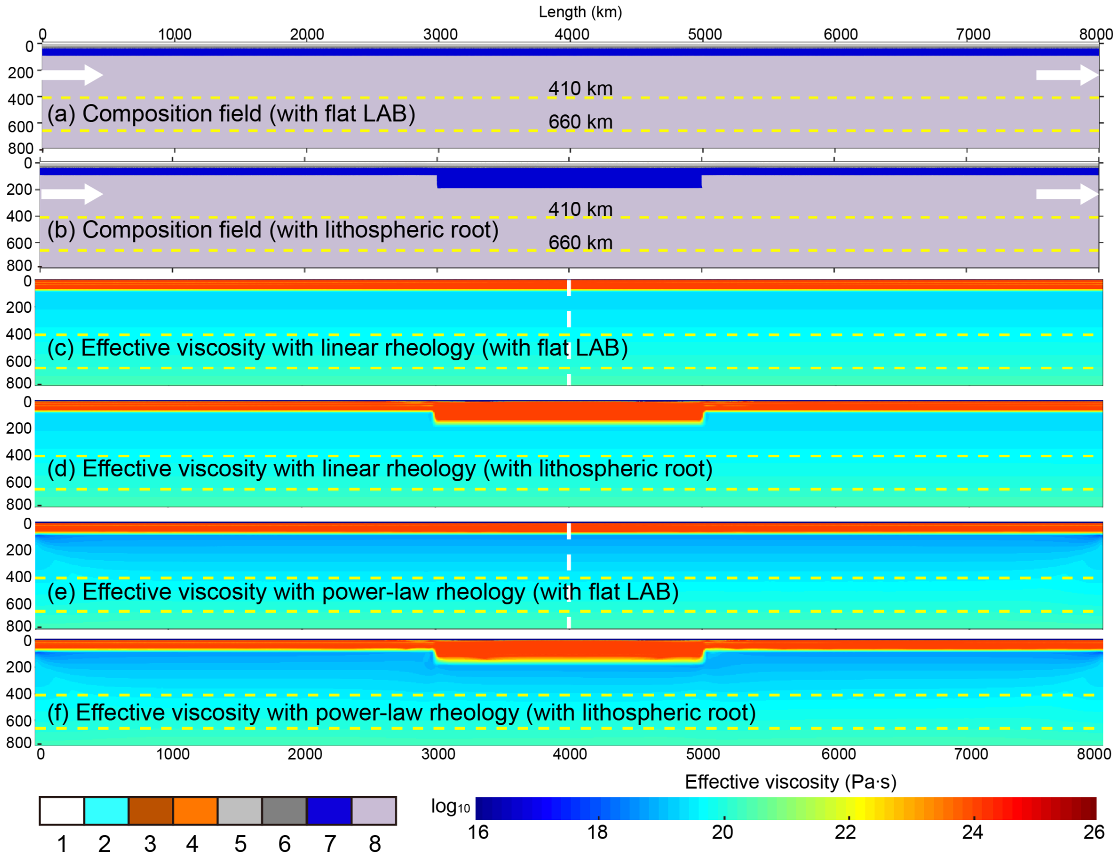

Figure S1. Model configuration. (a-b) Composition field with flat LAB or with a lithospheric root. The yellow dashed lines represent the phase transitions at 410 and 660 km in depth. The white arrows indicate the sub-plate mantle velocity configuration, with a value of 1 cm/yr in the models shown here. The colorbar at the bottom left corner indicates the composition field of the model: 1-sticky air; 2-sea water; 3,4-sediment; 5-continental upper crust; 6-continental lower crust; 7-lithospheric mantle; 8-asthenosphere. (c-d) Effective viscosity field with linear rheology. (e-f) Effective viscosity field with power-law rheology. The vertical white lines indicate the location of profiles shown in Figure S2.

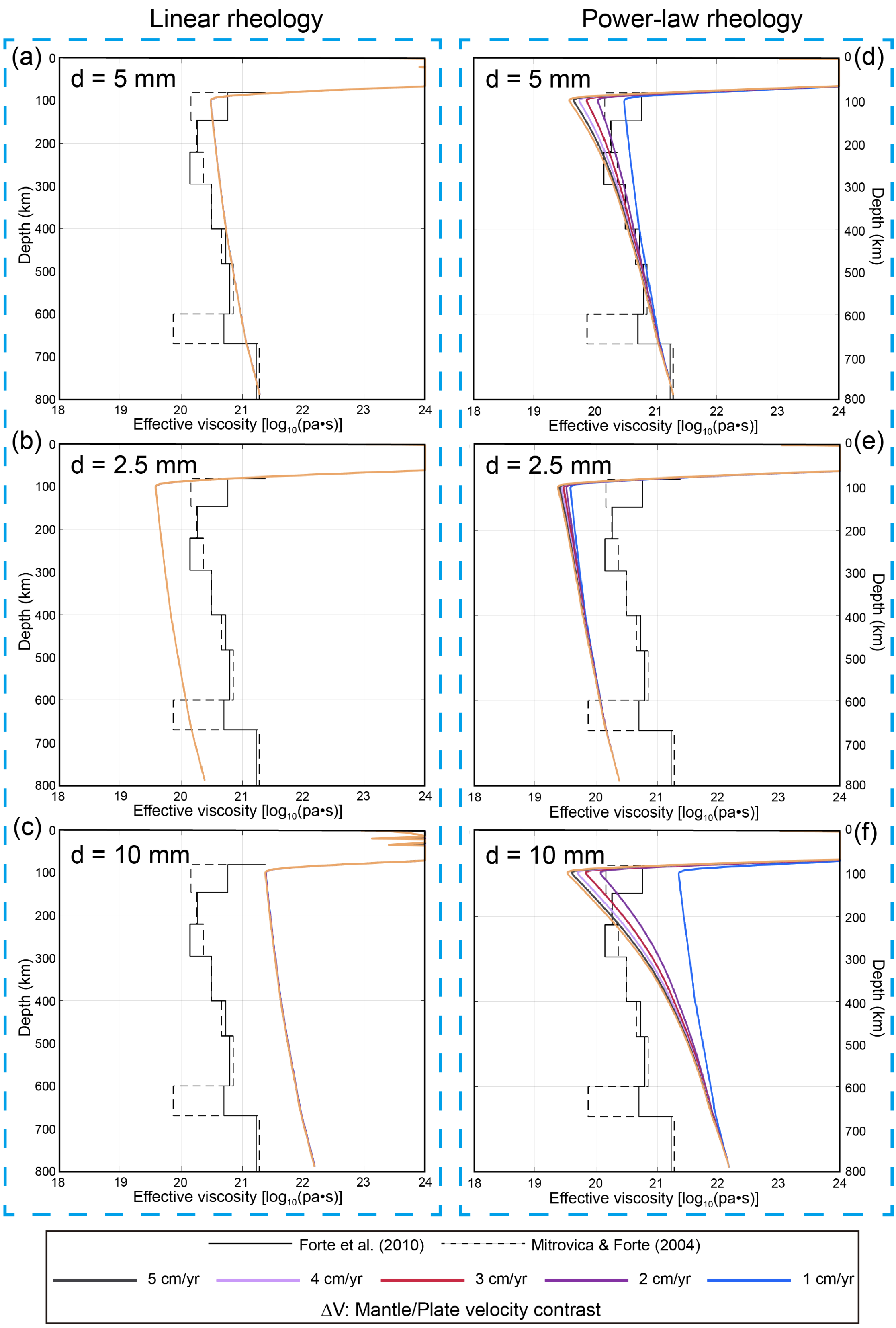

Figure S2. Comparison of effective viscosity profiles as indicated in Figure S1, with either linear (a-c) or power-law (d-f) rheology, and different grain sizes shown at the top left corner in each figure. The simulated profiles are compared to the sub-lithospheric mantle viscosity inferred from the joint inversions of glacial isostatic adjustment (GIA) data as well as the global convection observations (Forte et al., 2010; Mitrovica & Forte, 2004). The colored lines represent the models with variable mantle/plate velocity contrast as shown in the colorbar at the bottom.

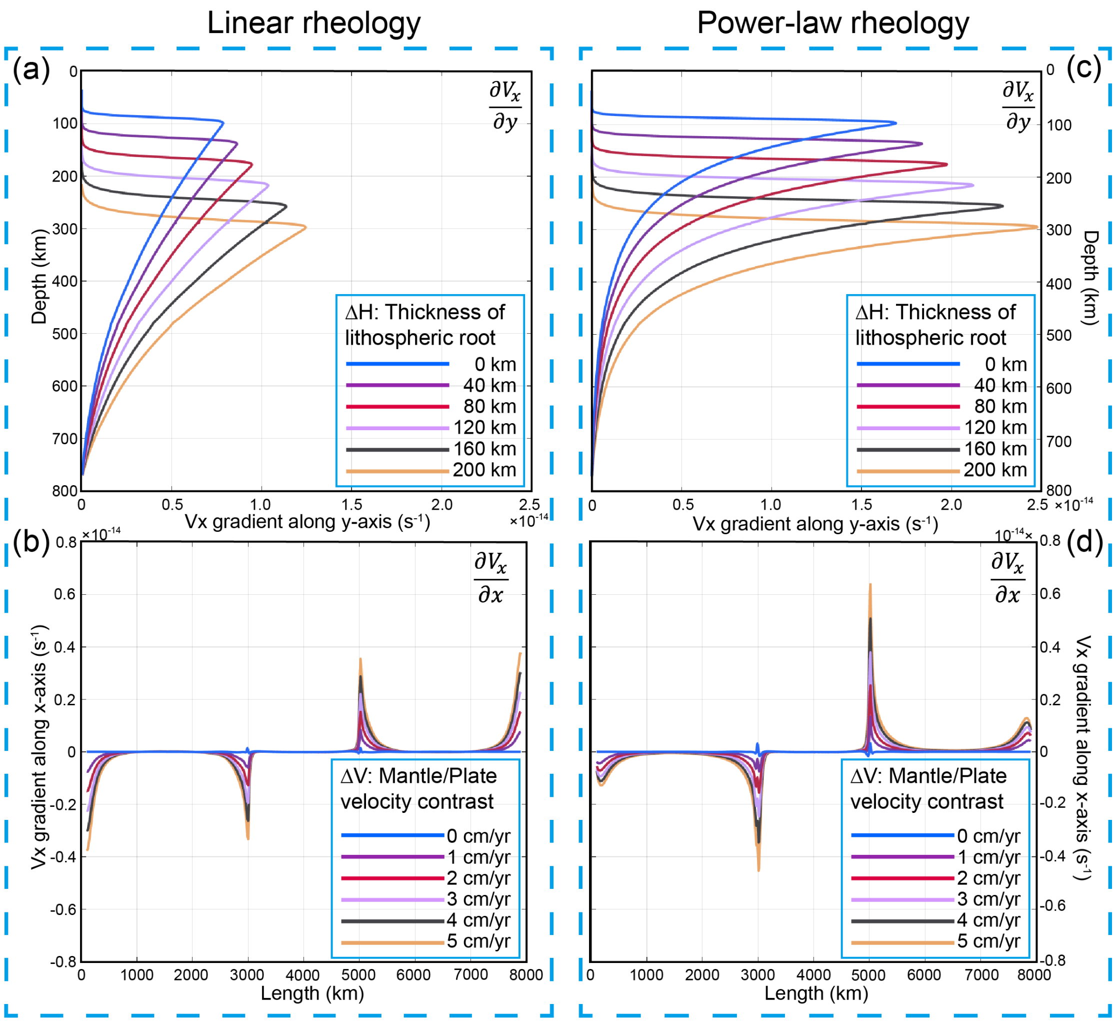

Figure S3. Method for dynamically defining the lithosphere-asthenosphere boundary (LAB) and the vertical walls of lithospheric root. (a) Profiles of $\frac{\partial V_x}{\partial y}$ along depth with linear rheology. (b) Profiles of $\frac{\partial V_x}{\partial x}$ along horizontal direction with linear rheology. (c) Profiles of $\frac{\partial V_x}{\partial y}$ along depth with power-law rheology. (d) Profiles of $\frac{\partial V_x}{\partial x}$ along horizontal direction with power-law rheology. The position of LAB is defined as the peak value of $\frac{\partial V_x}{\partial y}$ as shown in (a) and (c), whereas the position of vertical walls are defined as the peak values at around 3000 km (left wall) and 5000 km (right wall).

Different colors represent the models with variable mantle/plate velocity contrast or variable thickness of lithospheric root, as shown in the colorbar at the bottom right corner of each figure.

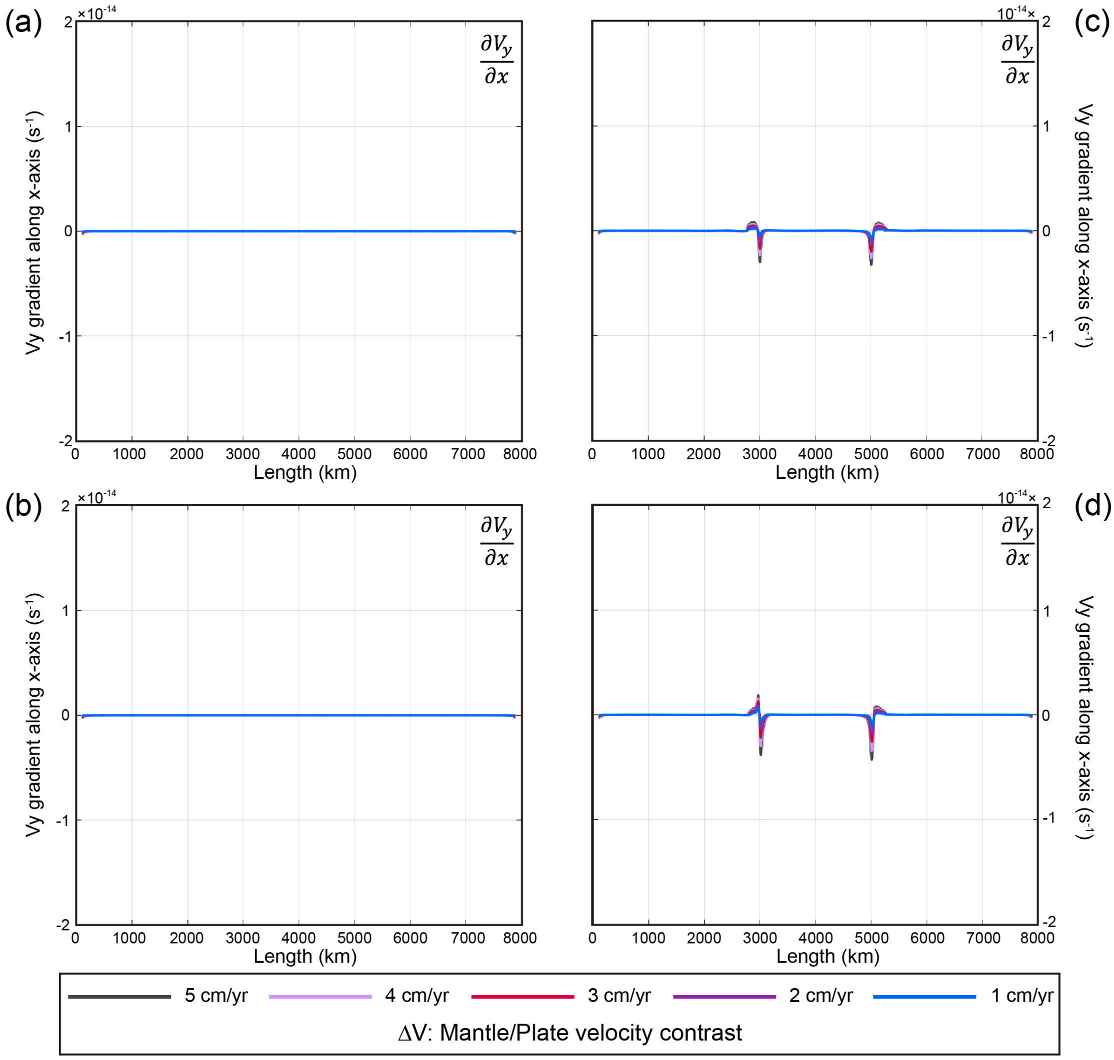

Figure S4. The negligible component of $\frac{\partial V_y}{\partial x}$ at the LAB in the models with (a) linear rheology and flat LAB (Figure 1b), (b) power-law rheology and flat LAB (Figure 1e), (c) linear rheology and a lithospheric root (Figure 2b), (d) power-law rheology and a lithospheric root (Figure 2e). It is worth noting that the $\frac{\partial V_y}{\partial x}$ value at the vertical walls of lithospheric roots are significant; however, the resulting shear stress by integrating over the horizontal x-direction is negligible.

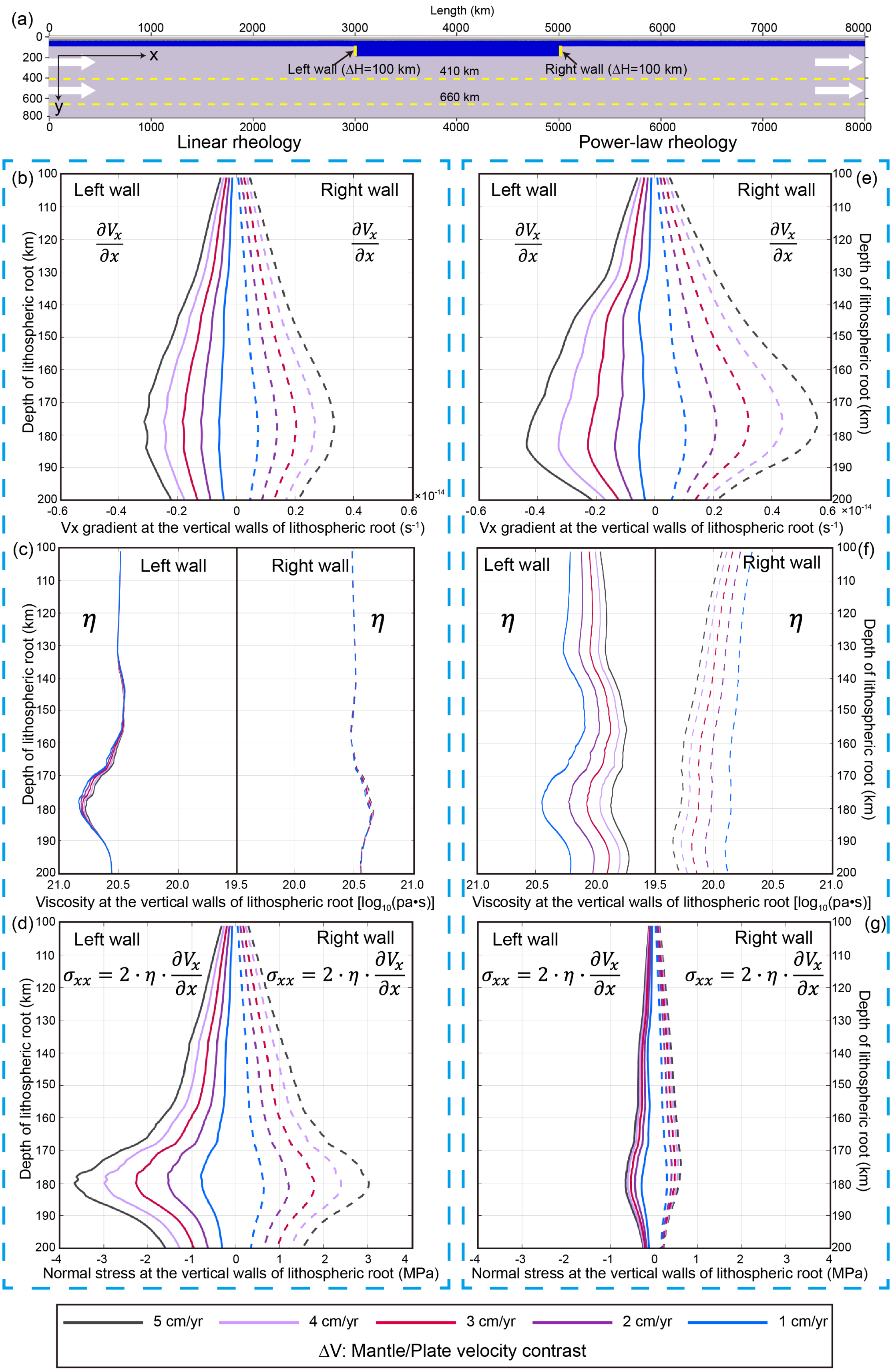

(a)
Length (km)
Left wall (ΔH=100 km)
Right wall (ΔH=100 km)
410 km
660 km
Linear rheology
Power-law rheology
(b) (c) (d) (e) (f) (g)
Left wall
Right wall
Depth of lithospheric root (km)
Vx gradient at the vertical walls of lithospheric root (s-1)
Viscosity at the vertical walls of lithospheric root [log10(pa•s)]
Normal stress at the vertical walls of lithospheric root (MPa)
$\sigma_{xx} = 2 \cdot \eta \cdot \frac{\partial V_x}{\partial x}$
5 cm/yr
4 cm/yr
3 cm/yr
2 cm/yr
1 cm/yr
ΔV: Mantle/Plate velocity contrast

Figure S5. Normal stress calculation at the vertical walls of lithospheric root, indicated by the yellow solid lines in (a), with either linear (b-d) or power-law (e-g) rheology. The solid and dashed lines represent the values at the left and right walls, respectively.

Table S1. Viscous flow law parameters used in the numerical models [a)].

Symbol	Flow law	$A_R(MPa^{-n} \cdot s^{-1})$	A_H	n	p	$E^*(kJ/mol)$	$V^*(10^{-6}m^3/mol)$
A*	Wet quartize	3.2×10^{-4}	-	2.3	-	154	8
B*	Plagioclase An_{75}	3.3×10^{-4}	-	3.2	-	238	8
C*	Diffusion creep of olivine	-	1.5×10^{9}	1	3	375	4.5
D*	Dislocation creep of olivine	-	1.1×10^{5}	3.5	0	530	11

[a)] Viscous parameters of crustal rocks (A* and B*) are from Kirby & Kronenberg (1987) and Ranalli (1995). Viscous parameters of mantle rocks (C*, D*) are from Hirth & Kohlstedt (2003)

Table S2. Material properties used in the numerical experiments [a)].

Material (state)	$\boldsymbol{\rho_0}$ $(kg \cdot m^{-3})$	$\boldsymbol{C_p}$ $(J \cdot kg^{-1} \cdot K^{-1})$	$\boldsymbol{k}$ [b)] $(W \cdot m^{-1} \cdot K^{-1})$	$\boldsymbol{T}_{\text{solidus}}$ [c)] (K)	$\boldsymbol{T}_{\text{liquius}}$ [d)] (K)	$\boldsymbol{Q_L}$ $(kJ \cdot kg^{-1})$	$\boldsymbol{H_r}$ $(\mu W \cdot m^{-3})$	**Viscous** [e)] Flow law	**Plastic** [f)] C_0(MPa)	**Plastic** [f)] $\sin(\varphi_{\text{eff}})$
Sticky air (1)	1	3.3×10^6	200	-	-	-	0	10^{18} Pa·s	-	-
Sticky water (2)	1000	3.3×10^3	200	-	-	-	0	10^{18} Pa·s	-	-
Sediment (3, 4)	2700	1000	K_1	T_{S1}	T_{L1}	300	2.0	A*	10~1	0.1~0.05
Continental upper crust (5)	2700	1000	K_1	T_{S1}	T_{L1}	300	1.0	A*	10~1	0.1~0.05
Continental lower crust (6)	2900	1000	K_1	T_{S2}	T_{L2}	380	1.0	B*	10~1	0.6~0.1
Lithospheric mantle (7)	3300	1000	K_2	T_{S3}	T_{L3}	400	0.022	C*+D*	10~1	0.6~0.1
Asthenosphere (8)	3300	1000	K_2	T_{S3}	T_{L3}	400	0.022	C*+D*	10~1	0.6~0.1
References [g)]	1,2	1,2	3	6,7	6,7	1,2	1	4,5	-	-

a) The thermal expansion coefficient $\alpha = 3 \times 10^{-5}\ \mathrm{K}^{-1}$ and the compressibility coefficient $\beta = 1 \times 10^{-5}\ \mathrm{MPa}^{-1}$ are used for all types.

b) $\mathrm{K}_1 = (0.64 + 807/(T_{\mathrm{K}} + 77)) \cdot \exp(0.00004 P_{\mathrm{MPa}})$; $\mathrm{K}_2 = (0.73 + 1293/(T_{\mathrm{K}} + 77)) \cdot \exp(0.00004 P_{\mathrm{MPa}})$.

c) $T_{S1} = \{889 + 17900/(P + 54) + 20200/(P + 54)^2\ at\ P < 1200\ \mathrm{MPa}\}$ or $\{831 + 0.06P\ at\ P > 1200\ \mathrm{MPa}\}$; $T_{S2} = 1327 + 0.0906P$; $T_{S3} =$ KATZ2003.

d) $T_{L1} = 1262 + 0.09P$; $T_{L2} = 1423 + 0.105P$; $T_{L3} =$ KATZ2003.

e) Parameters of viscous flow laws are shown in Table S1.

f) Strain weakening effect is included in plastic rheology, in which both cohesion C_0 and effective friction angle $\sin(\varphi_{\text{eff}})$ decrease with larger strain rate.

[g] References: 1-Turcotte & Schubert (2002); 2-Bittner & Schmeling (1995); 3-Clauser & Huenges (1995); 4-Ranalli (1995); 5-Hirth & Kohlstedt (2003); 6-Schmidt & Poli (1998); 7-Katz et al. (2003).

Table S3. Summary of the model parameters and results.

Model ID	Mantle Rheology	Mantle/plate velocity contrast (cm/yr)	Thickness of lithospheric root (km)	Grain size for mantle rheology (mm)	Shear force (N/m)	Normal force (N/m)	Whole mantle flow traction (N/m)
001	linear	1	0	5	1.63E+12	0.00E+00	1.63E+12
002	linear	1	20	5	1.71E+12	7.48E+09	1.72E+12
003	linear	1	40	5	1.80E+12	2.23E+10	1.82E+12
004	linear	1	60	5	1.90E+12	3.43E+10	1.93E+12
005	linear	1	80	5	2.00E+12	4.81E+10	2.05E+12
006	linear	1	100	5	2.12E+12	6.41E+10	2.18E+12
007	linear	1	120	5	2.24E+12	8.03E+10	2.32E+12
008	linear	1	140	5	2.39E+12	9.74E+10	2.48E+12
009	linear	1	160	5	2.54E+12	1.14E+11	2.66E+12
010	linear	1	180	5	2.71E+12	1.33E+11	2.84E+12
011	linear	1	200	5	2.89E+12	1.55E+11	3.04E+12
012	linear	2	0	5	3.24E+12	0.00E+00	3.24E+12
013	linear	2	20	5	3.41E+12	1.45E+10	3.43E+12
014	linear	2	40	5	3.60E+12	4.25E+10	3.64E+12
015	linear	2	60	5	3.79E+12	6.66E+10	3.86E+12
016	linear	2	80	5	4.01E+12	9.41E+10	4.10E+12
017	linear	2	100	5	4.24E+12	1.26E+11	4.37E+12
018	linear	2	120	5	4.50E+12	1.58E+11	4.66E+12
019	linear	2	140	5	4.78E+12	1.92E+11	4.97E+12
020	linear	2	160	5	5.09E+12	2.26E+11	5.32E+12
021	linear	2	180	5	5.43E+12	2.62E+11	5.69E+12
022	linear	2	200	5	5.80E+12	3.06E+11	6.10E+12
023	linear	3	0	5	4.83E+12	0.00E+00	4.83E+12
024	linear	3	20	5	5.09E+12	2.10E+10	5.12E+12
025	linear	3	40	5	5.37E+12	6.32E+10	5.43E+12
026	linear	3	60	5	5.66E+12	9.84E+10	5.76E+12
027	linear	3	80	5	5.98E+12	1.40E+11	6.12E+12
028	linear	3	100	5	6.33E+12	1.87E+11	6.52E+12
029	linear	3	120	5	6.72E+12	2.34E+11	6.95E+12
030	linear	3	140	5	7.13E+12	2.83E+11	7.42E+12
031	linear	3	160	5	7.61E+12	3.36E+11	7.94E+12
032	linear	3	180	5	8.10E+12	3.90E+11	8.49E+12
033	linear	3	200	5	8.65E+12	4.53E+11	9.10E+12

034	linear	4	0	5	6.41E+12	-2.54E+05	6.41E+12
035	linear	4	20	5	6.76E+12	3.01E+10	6.79E+12
036	linear	4	40	5	7.12E+12	8.31E+10	7.20E+12
037	linear	4	60	5	7.51E+12	1.30E+11	7.64E+12
038	linear	4	80	5	7.93E+12	1.85E+11	8.12E+12
039	linear	4	100	5	8.41E+12	2.44E+11	8.65E+12
040	linear	4	120	5	8.91E+12	3.07E+11	9.22E+12
041	linear	4	140	5	9.47E+12	3.75E+11	9.84E+12
042	linear	4	160	5	1.01E+13	4.44E+11	1.05E+13
043	linear	4	180	5	1.07E+13	5.16E+11	1.13E+13
044	linear	4	200	5	1.15E+13	5.98E+11	1.21E+13
045	linear	5	0	5	7.99E+12	0.00E+00	7.99E+12
046	linear	5	20	5	8.42E+12	3.75E+10	8.46E+12
047	linear	5	40	5	8.87E+12	1.03E+11	8.97E+12
048	linear	5	60	5	9.35E+12	1.61E+11	9.51E+12
049	linear	5	80	5	9.88E+12	2.27E+11	1.01E+13
050	linear	5	100	5	1.05E+13	3.04E+11	1.08E+13
051	linear	5	120	5	1.11E+13	3.82E+11	1.15E+13
052	linear	5	140	5	1.18E+13	4.66E+11	1.22E+13
053	linear	5	160	5	1.25E+13	5.52E+11	1.31E+13
054	linear	5	180	5	1.34E+13	6.41E+11	1.40E+13
055	linear	5	200	5	1.43E+13	7.43E+11	1.50E+13
056	linear	6	0	5	9.55E+12	0.00E+00	9.55E+12
057	linear	6	20	5	1.01E+13	4.50E+10	1.01E+13
058	linear	6	40	5	1.06E+13	1.23E+11	1.07E+13
059	linear	6	60	5	1.12E+13	1.93E+11	1.14E+13
060	linear	6	80	5	1.18E+13	2.72E+11	1.21E+13
061	linear	6	100	5	1.25E+13	3.63E+11	1.29E+13
062	linear	6	120	5	1.32E+13	4.56E+11	1.37E+13
063	linear	6	140	5	1.41E+13	5.56E+11	1.46E+13
064	linear	6	160	5	1.50E+13	6.59E+11	1.56E+13
065	linear	6	180	5	1.59E+13	7.65E+11	1.67E+13
066	linear	6	200	5	1.70E+13	8.77E+11	1.79E+13
067	linear	7	0	5	1.11E+13	0.00E+00	1.11E+13
068	linear	7	20	5	1.17E+13	5.26E+10	1.18E+13
069	linear	7	40	5	1.23E+13	1.43E+11	1.25E+13
070	linear	7	60	5	1.30E+13	2.22E+11	1.32E+13
071	linear	7	80	5	1.37E+13	3.16E+11	1.41E+13
072	linear	7	100	5	1.45E+13	4.23E+11	1.50E+13
073	linear	7	120	5	1.54E+13	5.31E+11	1.59E+13
074	linear	7	140	5	1.64E+13	6.47E+11	1.70E+13

075	linear	7	160	5	1.74E+13	7.66E+11	1.82E+13
076	linear	7	180	5	1.85E+13	8.88E+11	1.94E+13
077	linear	7	200	5	1.97E+13	1.02E+12	2.08E+13
078	linear	8	0	5	1.27E+13	0.00E+00	1.27E+13
079	linear	8	20	5	1.33E+13	6.01E+10	1.34E+13
080	linear	8	40	5	1.40E+13	1.62E+11	1.42E+13
081	linear	8	60	5	1.48E+13	2.53E+11	1.51E+13
082	linear	8	80	5	1.56E+13	3.61E+11	1.60E+13
083	linear	8	100	5	1.66E+13	4.82E+11	1.70E+13
084	linear	8	120	5	1.76E+13	6.06E+11	1.82E+13
085	linear	8	140	5	1.86E+13	7.36E+11	1.94E+13
086	linear	8	160	5	1.98E+13	8.73E+11	2.07E+13
087	linear	8	180	5	2.10E+13	1.01E+12	2.21E+13
088	linear	8	200	5	2.25E+13	1.16E+12	2.36E+13
089	linear	9	0	5	1.42E+13	0.00E+00	1.42E+13
090	linear	9	20	5	1.50E+13	6.77E+10	1.50E+13
091	linear	9	40	5	1.57E+13	1.79E+11	1.59E+13
092	linear	9	60	5	1.66E+13	2.85E+11	1.69E+13
093	linear	9	80	5	1.75E+13	4.06E+11	1.79E+13
094	linear	9	100	5	1.86E+13	5.41E+11	1.91E+13
095	linear	9	120	5	1.97E+13	6.80E+11	2.04E+13
096	linear	9	140	5	2.09E+13	8.26E+11	2.17E+13
097	linear	9	160	5	2.22E+13	9.80E+11	2.32E+13
098	linear	9	180	5	2.36E+13	1.13E+12	2.47E+13
099	linear	9	200	5	2.51E+13	1.30E+12	2.64E+13
100	linear	10	0	5	1.57E+13	0.00E+00	1.57E+13
101	linear	10	20	5	1.66E+13	7.52E+10	1.67E+13
102	linear	10	40	5	1.75E+13	1.99E+11	1.77E+13
103	linear	10	60	5	1.84E+13	3.16E+11	1.87E+13
104	linear	10	80	5	1.95E+13	4.51E+11	1.99E+13
105	linear	10	100	5	2.06E+13	6.00E+11	2.12E+13
106	linear	10	120	5	2.18E+13	7.54E+11	2.25E+13
107	linear	10	140	5	2.31E+13	9.15E+11	2.40E+13
108	linear	10	160	5	2.46E+13	1.09E+12	2.57E+13
109	linear	10	180	5	2.61E+13	1.26E+12	2.74E+13
110	linear	10	200	5	2.78E+13	1.44E+12	2.92E+13
111	power-law	1	0	5	8.88E+11	0.00E+00	8.88E+11
112	power-law	1	20	5	9.33E+11	3.79E+09	9.37E+11
113	power-law	1	40	5	9.81E+11	1.19E+10	9.93E+11
114	power-law	1	60	5	1.04E+12	1.66E+10	1.05E+12
115	power-law	1	80	5	1.09E+12	2.26E+10	1.12E+12

116	power-law	1	100	5	1.16E+12	3.02E+10	1.19E+12
117	power-law	1	120	5	1.22E+12	3.78E+10	1.26E+12
118	power-law	1	140	5	1.30E+12	4.61E+10	1.35E+12
119	power-law	1	160	5	1.38E+12	5.50E+10	1.44E+12
120	power-law	1	180	5	1.47E+12	6.41E+10	1.54E+12
121	power-law	1	200	5	1.57E+12	7.45E+10	1.65E+12
122	power-law	2	0	5	1.35E+12	0.00E+00	1.35E+12
123	power-law	2	20	5	1.42E+12	5.34E+09	1.43E+12
124	power-law	2	40	5	1.50E+12	1.69E+10	1.52E+12
125	power-law	2	60	5	1.59E+12	2.50E+10	1.61E+12
126	power-law	2	80	5	1.68E+12	3.47E+10	1.71E+12
127	power-law	2	100	5	1.78E+12	4.65E+10	1.82E+12
128	power-law	2	120	5	1.89E+12	5.81E+10	1.95E+12
129	power-law	2	140	5	2.01E+12	7.12E+10	2.08E+12
130	power-law	2	160	5	2.14E+12	8.51E+10	2.23E+12
131	power-law	2	180	5	2.28E+12	1.00E+11	2.38E+12
132	power-law	2	200	5	2.44E+12	1.17E+11	2.56E+12
133	power-law	3	0	5	1.67E+12	0.00E+00	1.67E+12
134	power-law	3	20	5	1.77E+12	6.23E+09	1.78E+12
135	power-law	3	40	5	1.86E+12	2.03E+10	1.89E+12
136	power-law	3	60	5	1.97E+12	3.07E+10	2.00E+12
137	power-law	3	80	5	2.09E+12	4.31E+10	2.13E+12
138	power-law	3	100	5	2.21E+12	5.73E+10	2.27E+12
139	power-law	3	120	5	2.35E+12	7.23E+10	2.42E+12
140	power-law	3	140	5	2.50E+12	8.87E+10	2.59E+12
141	power-law	3	160	5	2.67E+12	1.06E+11	2.77E+12
142	power-law	3	180	5	2.85E+12	1.25E+11	2.97E+12
143	power-law	3	200	5	3.05E+12	1.46E+11	3.20E+12
144	power-law	4	0	5	1.93E+12	0.00E+00	1.93E+12
145	power-law	4	20	5	2.04E+12	7.00E+09	2.04E+12
146	power-law	4	40	5	2.15E+12	2.29E+10	2.17E+12
147	power-law	4	60	5	2.27E+12	3.51E+10	2.30E+12
148	power-law	4	80	5	2.41E+12	4.91E+10	2.46E+12
149	power-law	4	100	5	2.55E+12	6.59E+10	2.62E+12
150	power-law	4	120	5	2.71E+12	8.33E+10	2.80E+12
151	power-law	4	140	5	2.89E+12	1.02E+11	2.99E+12
152	power-law	4	160	5	3.07E+12	1.22E+11	3.20E+12
153	power-law	4	180	5	3.29E+12	1.44E+11	3.43E+12
154	power-law	4	200	5	3.53E+12	1.68E+11	3.69E+12
155	power-law	5	0	5	2.14E+12	0.00E+00	2.14E+12
156	power-law	5	20	5	2.26E+12	7.64E+09	2.27E+12

157	power-law	5	40	5	2.38E+12	2.50E+10	2.41E+12
158	power-law	5	60	5	2.52E+12	3.86E+10	2.56E+12
159	power-law	5	80	5	2.67E+12	5.43E+10	2.73E+12
160	power-law	5	100	5	2.83E+12	7.29E+10	2.91E+12
161	power-law	5	120	5	3.01E+12	9.21E+10	3.10E+12
162	power-law	5	140	5	3.20E+12	1.13E+11	3.32E+12
163	power-law	5	160	5	3.42E+12	1.35E+11	3.55E+12
164	power-law	5	180	5	3.65E+12	1.59E+11	3.81E+12
165	power-law	5	200	5	3.91E+12	1.86E+11	4.10E+12
166	power-law	6	0	5	2.32E+12	0.00E+00	2.32E+12
167	power-law	6	20	5	2.45E+12	8.18E+09	2.46E+12
168	power-law	6	40	5	2.58E+12	2.67E+10	2.61E+12
169	power-law	6	60	5	2.74E+12	4.13E+10	2.78E+12
170	power-law	6	80	5	2.90E+12	5.87E+10	2.96E+12
171	power-law	6	100	5	3.07E+12	7.89E+10	3.15E+12
172	power-law	6	120	5	3.26E+12	9.97E+10	3.36E+12
173	power-law	6	140	5	3.48E+12	1.22E+11	3.60E+12
174	power-law	6	160	5	3.71E+12	1.46E+11	3.85E+12
175	power-law	6	180	5	3.96E+12	1.72E+11	4.14E+12
176	power-law	6	200	5	4.25E+12	2.01E+11	4.45E+12
177	power-law	7	0	5	2.48E+12	0.00E+00	2.48E+12
178	power-law	7	20	5	2.61E+12	8.64E+09	2.62E+12
179	power-law	7	40	5	2.76E+12	2.83E+10	2.79E+12
180	power-law	7	60	5	2.92E+12	4.39E+10	2.97E+12
181	power-law	7	80	5	3.09E+12	6.26E+10	3.16E+12
182	power-law	7	100	5	3.28E+12	8.40E+10	3.36E+12
183	power-law	7	120	5	3.49E+12	1.06E+11	3.59E+12
184	power-law	7	140	5	3.71E+12	1.30E+11	3.85E+12
185	power-law	7	160	5	3.97E+12	1.55E+11	4.12E+12
186	power-law	7	180	5	4.24E+12	1.83E+11	4.42E+12
187	power-law	7	200	5	4.55E+12	2.13E+11	4.76E+12
188	power-law	8	0	5	2.62E+12	0.00E+00	2.62E+12
189	power-law	8	20	5	2.76E+12	9.06E+09	2.77E+12
190	power-law	8	40	5	2.92E+12	2.96E+10	2.95E+12
191	power-law	8	60	5	3.09E+12	4.62E+10	3.13E+12
192	power-law	8	80	5	3.27E+12	6.61E+10	3.33E+12
193	power-law	8	100	5	3.47E+12	8.86E+10	3.55E+12
194	power-law	8	120	5	3.68E+12	1.12E+11	3.80E+12
195	power-law	8	140	5	3.93E+12	1.37E+11	4.06E+12
196	power-law	8	160	5	4.19E+12	1.64E+11	4.36E+12
197	power-law	8	180	5	4.48E+12	1.93E+11	4.67E+12

198	power-law	8	200	5	4.80E+12	2.25E+11	5.03E+12
199	power-law	9	0	5	2.75E+12	0.00E+00	2.75E+12
200	power-law	9	20	5	2.90E+12	9.43E+09	2.91E+12
201	power-law	9	40	5	3.06E+12	3.05E+10	3.09E+12
202	power-law	9	60	5	3.24E+12	4.83E+10	3.29E+12
203	power-law	9	80	5	3.43E+12	6.92E+10	3.50E+12
204	power-law	9	100	5	3.64E+12	9.27E+10	3.73E+12
205	power-law	9	120	5	3.86E+12	1.17E+11	3.98E+12
206	power-law	9	140	5	4.12E+12	1.43E+11	4.26E+12
207	power-law	9	160	5	4.39E+12	1.72E+11	4.56E+12
208	power-law	9	180	5	4.69E+12	2.02E+11	4.90E+12
209	power-law	9	200	5	5.03E+12	2.36E+11	5.27E+12
210	power-law	10	0	5	2.86E+12	0.00E+00	2.86E+12
211	power-law	10	20	5	3.02E+12	9.78E+09	3.03E+12
212	power-law	10	40	5	3.20E+12	3.15E+10	3.23E+12
213	power-law	10	60	5	3.38E+12	5.02E+10	3.43E+12
214	power-law	10	80	5	3.58E+12	7.20E+10	3.65E+12
215	power-law	10	100	5	3.79E+12	9.65E+10	3.89E+12
216	power-law	10	120	5	4.04E+12	1.22E+11	4.16E+12
217	power-law	10	140	5	4.30E+12	1.49E+11	4.45E+12
218	power-law	10	160	5	4.59E+12	1.78E+11	4.77E+12
219	power-law	10	180	5	4.90E+12	2.10E+11	5.11E+12
220	power-law	10	200	5	5.26E+12	2.45E+11	5.50E+12
221	linear	1	0	2.5	2.15E+11	0.00E+00	2.15E+11
222	linear	1	20	2.5	2.26E+11	1.57E+09	2.28E+11
223	linear	1	40	2.5	2.39E+11	7.39E+09	2.47E+11
224	linear	1	60	2.5	2.53E+11	1.20E+10	2.65E+11
225	linear	1	80	2.5	2.68E+11	1.01E+10	2.78E+11
226	linear	1	100	2.5	2.86E+11	1.15E+10	2.98E+11
227	linear	1	120	2.5	3.06E+11	1.44E+10	3.20E+11
228	linear	1	140	2.5	3.28E+11	1.72E+10	3.45E+11
229	linear	1	160	2.5	3.52E+11	2.01E+10	3.72E+11
230	linear	1	180	2.5	3.81E+11	2.39E+10	4.05E+11
231	linear	1	200	2.5	4.12E+11	2.73E+10	4.40E+11
232	linear	2	0	2.5	4.30E+11	0.00E+00	4.30E+11
233	linear	2	20	2.5	4.54E+11	2.36E+09	4.56E+11
234	linear	2	40	2.5	4.80E+11	9.75E+09	4.90E+11
235	linear	2	60	2.5	5.09E+11	1.63E+10	5.26E+11
236	linear	2	80	2.5	5.41E+11	1.60E+10	5.57E+11
237	linear	2	100	2.5	5.77E+11	1.96E+10	5.96E+11
238	linear	2	120	2.5	6.17E+11	2.50E+10	6.42E+11

239	linear	2	140	2.5	6.62E+11	3.03E+10	6.93E+11
240	linear	2	160	2.5	7.12E+11	3.57E+10	7.48E+11
241	linear	2	180	2.5	7.70E+11	4.24E+10	8.12E+11
242	linear	2	200	2.5	8.34E+11	4.92E+10	8.83E+11
243	linear	3	0	2.5	6.44E+11	0.00E+00	6.44E+11
244	linear	3	20	2.5	6.82E+11	3.19E+09	6.85E+11
245	linear	3	40	2.5	7.21E+11	1.29E+10	7.34E+11
246	linear	3	60	2.5	7.65E+11	2.05E+10	7.85E+11
247	linear	3	80	2.5	8.14E+11	2.19E+10	8.35E+11
248	linear	3	100	2.5	8.68E+11	2.77E+10	8.95E+11
249	linear	3	120	2.5	9.28E+11	3.56E+10	9.64E+11
250	linear	3	140	2.5	9.96E+11	4.31E+10	1.04E+12
251	linear	3	160	2.5	1.07E+12	5.14E+10	1.13E+12
252	linear	3	180	2.5	1.16E+12	6.09E+10	1.22E+12
253	linear	3	200	2.5	1.26E+12	7.10E+10	1.33E+12
254	linear	4	0	2.5	8.59E+11	3.63E+05	8.59E+11
255	linear	4	20	2.5	9.09E+11	4.38E+09	9.13E+11
256	linear	4	40	2.5	9.62E+11	1.57E+10	9.78E+11
257	linear	4	60	2.5	1.02E+12	2.47E+10	1.04E+12
258	linear	4	80	2.5	1.08E+12	2.78E+10	1.11E+12
259	linear	4	100	2.5	1.16E+12	3.55E+10	1.19E+12
260	linear	4	120	2.5	1.24E+12	4.57E+10	1.28E+12
261	linear	4	140	2.5	1.33E+12	5.61E+10	1.39E+12
262	linear	4	160	2.5	1.44E+12	6.71E+10	1.50E+12
263	linear	4	180	2.5	1.55E+12	7.95E+10	1.63E+12
264	linear	4	200	2.5	1.68E+12	9.28E+10	1.77E+12
265	linear	5	0	2.5	1.07E+12	0.00E+00	1.07E+12
266	linear	5	20	2.5	1.14E+12	5.33E+09	1.14E+12
267	linear	5	40	2.5	1.20E+12	1.84E+10	1.22E+12
268	linear	5	60	2.5	1.28E+12	2.89E+10	1.31E+12
269	linear	5	80	2.5	1.36E+12	3.33E+10	1.39E+12
270	linear	5	100	2.5	1.45E+12	4.36E+10	1.49E+12
271	linear	5	120	2.5	1.55E+12	5.62E+10	1.61E+12
272	linear	5	140	2.5	1.67E+12	6.91E+10	1.73E+12
273	linear	5	160	2.5	1.80E+12	8.27E+10	1.88E+12
274	linear	5	180	2.5	1.94E+12	9.81E+10	2.04E+12
275	linear	5	200	2.5	2.11E+12	1.14E+11	2.22E+12
276	linear	6	0	2.5	1.29E+12	0.00E+00	1.29E+12
277	linear	6	20	2.5	1.36E+12	6.29E+09	1.37E+12
278	linear	6	40	2.5	1.44E+12	2.11E+10	1.46E+12
279	linear	6	60	2.5	1.53E+12	3.31E+10	1.56E+12

280	linear	6	80	2.5	1.63E+12	3.91E+10	1.67E+12
281	linear	6	100	2.5	1.74E+12	5.17E+10	1.79E+12
282	linear	6	120	2.5	1.86E+12	6.67E+10	1.93E+12
283	linear	6	140	2.5	2.00E+12	8.21E+10	2.08E+12
284	linear	6	160	2.5	2.16E+12	9.83E+10	2.25E+12
285	linear	6	180	2.5	2.33E+12	1.17E+11	2.44E+12
286	linear	6	200	2.5	2.53E+12	1.36E+11	2.66E+12
287	linear	7	0	2.5	1.50E+12	0.00E+00	1.50E+12
288	linear	7	20	2.5	1.59E+12	7.24E+09	1.60E+12
289	linear	7	40	2.5	1.68E+12	2.38E+10	1.71E+12
290	linear	7	60	2.5	1.79E+12	3.68E+10	1.82E+12
291	linear	7	80	2.5	1.90E+12	4.49E+10	1.95E+12
292	linear	7	100	2.5	2.03E+12	5.98E+10	2.09E+12
293	linear	7	120	2.5	2.17E+12	7.72E+10	2.25E+12
294	linear	7	140	2.5	2.33E+12	9.51E+10	2.43E+12
295	linear	7	160	2.5	2.51E+12	1.14E+11	2.63E+12
296	linear	7	180	2.5	2.71E+12	1.36E+11	2.85E+12
297	linear	7	200	2.5	2.95E+12	1.57E+11	3.11E+12
298	linear	8	0	2.5	1.72E+12	0.00E+00	1.72E+12
299	linear	8	20	2.5	1.82E+12	8.20E+09	1.82E+12
300	linear	8	40	2.5	1.92E+12	2.65E+10	1.95E+12
301	linear	8	60	2.5	2.04E+12	4.10E+10	2.08E+12
302	linear	8	80	2.5	2.17E+12	5.07E+10	2.22E+12
303	linear	8	100	2.5	2.32E+12	6.79E+10	2.38E+12
304	linear	8	120	2.5	2.48E+12	8.77E+10	2.57E+12
305	linear	8	140	2.5	2.66E+12	1.08E+11	2.77E+12
306	linear	8	160	2.5	2.87E+12	1.30E+11	3.00E+12
307	linear	8	180	2.5	3.10E+12	1.54E+11	3.26E+12
308	linear	8	200	2.5	3.37E+12	1.79E+11	3.55E+12
309	linear	9	0	2.5	1.93E+12	0.00E+00	1.93E+12
310	linear	9	20	2.5	2.04E+12	9.15E+09	2.05E+12
311	linear	9	40	2.5	2.16E+12	2.88E+10	2.19E+12
312	linear	9	60	2.5	2.30E+12	4.51E+10	2.34E+12
313	linear	9	80	2.5	2.44E+12	5.65E+10	2.50E+12
314	linear	9	100	2.5	2.60E+12	7.60E+10	2.68E+12
315	linear	9	120	2.5	2.79E+12	9.83E+10	2.89E+12
316	linear	9	140	2.5	2.99E+12	1.21E+11	3.12E+12
317	linear	9	160	2.5	3.23E+12	1.44E+11	3.38E+12
318	linear	9	180	2.5	3.49E+12	1.72E+11	3.66E+12
319	linear	9	200	2.5	3.79E+12	2.01E+11	3.99E+12
320	linear	10	0	2.5	2.14E+12	0.00E+00	2.14E+12

321	linear	10	20	2.5	2.27E+12	1.01E+10	2.28E+12
322	linear	10	40	2.5	2.41E+12	3.15E+10	2.44E+12
323	linear	10	60	2.5	2.55E+12	4.92E+10	2.60E+12
324	linear	10	80	2.5	2.72E+12	6.24E+10	2.78E+12
325	linear	10	100	2.5	2.90E+12	8.41E+10	2.98E+12
326	linear	10	120	2.5	3.10E+12	1.09E+11	3.21E+12
327	linear	10	140	2.5	3.33E+12	1.33E+11	3.46E+12
328	linear	10	160	2.5	3.59E+12	1.60E+11	3.75E+12
329	linear	10	180	2.5	3.88E+12	1.90E+11	4.07E+12
330	linear	10	200	2.5	4.21E+12	2.23E+11	4.43E+12
331	power-law	1	0	2.5	1.94E+11	2.22E+05	1.94E+11
332	power-law	1	20	2.5	2.05E+11	1.42E+09	2.06E+11
333	power-law	1	40	2.5	2.19E+11	7.22E+09	2.26E+11
334	power-law	1	60	2.5	2.31E+11	1.22E+10	2.43E+11
335	power-law	1	80	2.5	2.40E+11	9.98E+09	2.50E+11
336	power-law	1	100	2.5	2.53E+11	9.79E+09	2.63E+11
337	power-law	1	120	2.5	2.69E+11	1.21E+10	2.81E+11
338	power-law	1	140	2.5	2.89E+11	1.40E+10	3.03E+11
339	power-law	1	160	2.5	3.10E+11	1.63E+10	3.26E+11
340	power-law	1	180	2.5	3.59E+11	1.93E+10	3.79E+11
341	power-law	1	200	2.5	3.70E+11	2.17E+10	3.91E+11
342	power-law	2	0	2.5	3.66E+11	0.00E+00	3.66E+11
343	power-law	2	20	2.5	3.86E+11	2.13E+09	3.88E+11
344	power-law	2	40	2.5	4.07E+11	9.40E+09	4.17E+11
345	power-law	2	60	2.5	4.32E+11	1.56E+10	4.47E+11
346	power-law	2	80	2.5	4.59E+11	1.44E+10	4.73E+11
347	power-law	2	100	2.5	4.88E+11	1.59E+10	5.04E+11
348	power-law	2	120	2.5	5.21E+11	1.99E+10	5.41E+11
349	power-law	2	140	2.5	5.58E+11	2.38E+10	5.82E+11
350	power-law	2	160	2.5	5.98E+11	2.81E+10	6.26E+11
351	power-law	2	180	2.5	6.44E+11	3.32E+10	6.77E+11
352	power-law	2	200	2.5	6.98E+11	3.79E+10	7.35E+11
353	power-law	3	0	2.5	5.22E+11	0.00E+00	5.22E+11
354	power-law	3	20	2.5	5.51E+11	2.76E+09	5.54E+11
355	power-law	3	40	2.5	5.82E+11	1.13E+10	5.94E+11
356	power-law	3	60	2.5	6.17E+11	1.85E+10	6.36E+11
357	power-law	3	80	2.5	6.55E+11	1.84E+10	6.73E+11
358	power-law	3	100	2.5	6.97E+11	2.14E+10	7.19E+11
359	power-law	3	120	2.5	7.43E+11	2.71E+10	7.71E+11
360	power-law	3	140	2.5	7.96E+11	3.27E+10	8.28E+11
361	power-law	3	160	2.5	8.54E+11	3.88E+10	8.93E+11

362	power-law	3	180	2.5	9.20E+11	4.59E+10	9.66E+11
363	power-law	3	200	2.5	9.96E+11	5.26E+10	1.05E+12
364	power-law	4	0	2.5	6.65E+11	0.00E+00	6.65E+11
365	power-law	4	20	2.5	7.03E+11	3.33E+09	7.06E+11
366	power-law	4	40	2.5	7.44E+11	1.29E+10	7.57E+11
367	power-law	4	60	2.5	7.87E+11	2.12E+10	8.09E+11
368	power-law	4	80	2.5	8.36E+11	2.22E+10	8.58E+11
369	power-law	4	100	2.5	8.89E+11	2.66E+10	9.16E+11
370	power-law	4	120	2.5	9.49E+11	3.38E+10	9.83E+11
371	power-law	4	140	2.5	1.02E+12	4.05E+10	1.06E+12
372	power-law	4	160	2.5	1.09E+12	4.82E+10	1.14E+12
373	power-law	4	180	2.5	1.18E+12	5.72E+10	1.23E+12
374	power-law	4	200	2.5	1.27E+12	6.62E+10	1.34E+12
375	power-law	5	0	2.5	7.99E+11	0.00E+00	7.99E+11
376	power-law	5	20	2.5	8.45E+11	3.76E+09	8.49E+11
377	power-law	5	40	2.5	8.93E+11	1.45E+10	9.08E+11
378	power-law	5	60	2.5	9.46E+11	2.37E+10	9.70E+11
379	power-law	5	80	2.5	1.00E+12	2.56E+10	1.03E+12
380	power-law	5	100	2.5	1.07E+12	3.14E+10	1.10E+12
381	power-law	5	120	2.5	1.14E+12	3.96E+10	1.18E+12
382	power-law	5	140	2.5	1.22E+12	4.81E+10	1.27E+12
383	power-law	5	160	2.5	1.31E+12	5.73E+10	1.37E+12
384	power-law	5	180	2.5	1.41E+12	6.79E+10	1.48E+12
385	power-law	5	200	2.5	1.52E+12	7.88E+10	1.60E+12
386	power-law	6	0	2.5	9.27E+11	0.00E+00	9.27E+11
387	power-law	6	20	2.5	9.79E+11	4.23E+09	9.83E+11
388	power-law	6	40	2.5	1.03E+12	1.60E+10	1.05E+12
389	power-law	6	60	2.5	1.10E+12	2.61E+10	1.12E+12
390	power-law	6	80	2.5	1.16E+12	2.86E+10	1.19E+12
391	power-law	6	100	2.5	1.24E+12	3.55E+10	1.27E+12
392	power-law	6	120	2.5	1.32E+12	4.53E+10	1.37E+12
393	power-law	6	140	2.5	1.41E+12	5.51E+10	1.47E+12
394	power-law	6	160	2.5	1.52E+12	6.58E+10	1.58E+12
395	power-law	6	180	2.5	1.63E+12	7.81E+10	1.71E+12
396	power-law	6	200	2.5	1.76E+12	9.08E+10	1.85E+12
397	power-law	7	0	2.5	1.05E+12	0.00E+00	1.05E+12
398	power-law	7	20	2.5	1.10E+12	4.67E+09	1.11E+12
399	power-law	7	40	2.5	1.17E+12	1.73E+10	1.18E+12
400	power-law	7	60	2.5	1.24E+12	2.83E+10	1.26E+12
401	power-law	7	80	2.5	1.31E+12	3.16E+10	1.34E+12
402	power-law	7	100	2.5	1.40E+12	3.97E+10	1.44E+12

403	power-law	7	120	2.5	1.49E+12	5.08E+10	1.54E+12
404	power-law	7	140	2.5	1.59E+12	6.18E+10	1.65E+12
405	power-law	7	160	2.5	1.71E+12	7.39E+10	1.78E+12
406	power-law	7	180	2.5	1.84E+12	8.76E+10	1.93E+12
407	power-law	7	200	2.5	1.98E+12	1.02E+11	2.08E+12
408	power-law	8	0	2.5	1.16E+12	0.00E+00	1.16E+12
409	power-law	8	20	2.5	1.22E+12	5.08E+09	1.23E+12
410	power-law	8	40	2.5	1.29E+12	1.86E+10	1.31E+12
411	power-law	8	60	2.5	1.37E+12	3.01E+10	1.40E+12
412	power-law	8	80	2.5	1.45E+12	3.45E+10	1.49E+12
413	power-law	8	100	2.5	1.54E+12	4.36E+10	1.59E+12
414	power-law	8	120	2.5	1.65E+12	5.59E+10	1.70E+12
415	power-law	8	140	2.5	1.76E+12	6.81E+10	1.83E+12
416	power-law	8	160	2.5	1.89E+12	8.15E+10	1.97E+12
417	power-law	8	180	2.5	2.03E+12	9.66E+10	2.13E+12
418	power-law	8	200	2.5	2.20E+12	1.11E+11	2.31E+12
419	power-law	9	0	2.5	1.26E+12	0.00E+00	1.26E+12
420	power-law	9	20	2.5	1.33E+12	5.47E+09	1.34E+12
421	power-law	9	40	2.5	1.41E+12	1.96E+10	1.43E+12
422	power-law	9	60	2.5	1.49E+12	3.21E+10	1.53E+12
423	power-law	9	80	2.5	1.58E+12	3.72E+10	1.62E+12
424	power-law	9	100	2.5	1.69E+12	4.74E+10	1.73E+12
425	power-law	9	120	2.5	1.80E+12	6.08E+10	1.86E+12
426	power-law	9	140	2.5	1.92E+12	7.41E+10	2.00E+12
427	power-law	9	160	2.5	2.06E+12	8.87E+10	2.15E+12
428	power-law	9	180	2.5	2.22E+12	1.04E+11	2.32E+12
429	power-law	9	200	2.5	2.40E+12	1.21E+11	2.52E+12
430	power-law	10	0	2.5	1.36E+12	0.00E+00	1.36E+12
431	power-law	10	20	2.5	1.44E+12	5.84E+09	1.45E+12
432	power-law	10	40	2.5	1.53E+12	2.08E+10	1.55E+12
433	power-law	10	60	2.5	1.62E+12	3.39E+10	1.65E+12
434	power-law	10	80	2.5	1.71E+12	3.98E+10	1.75E+12
435	power-law	10	100	2.5	1.82E+12	5.10E+10	1.87E+12
436	power-law	10	120	2.5	1.94E+12	6.54E+10	2.01E+12
437	power-law	10	140	2.5	2.08E+12	7.97E+10	2.16E+12
438	power-law	10	160	2.5	2.23E+12	9.49E+10	2.32E+12
439	power-law	10	180	2.5	2.40E+12	1.12E+11	2.51E+12
440	power-law	10	200	2.5	2.59E+12	1.31E+11	2.72E+12
441	linear	1	0	10	8.54E+12	0.00E+00	8.54E+12
442	linear	1	20	10	8.81E+12	3.43E+10	8.85E+12
443	linear	1	40	10	9.07E+12	9.28E+10	9.17E+12

444	linear	1	60	10	9.33E+12	1.41E+11	9.47E+12
445	linear	1	80	10	9.54E+12	1.88E+11	9.73E+12
446	linear	1	100	10	9.79E+12	2.39E+11	1.00E+13
447	linear	1	120	10	1.00E+13	2.87E+11	1.03E+13
448	linear	1	140	10	1.02E+13	3.31E+11	1.05E+13
449	linear	1	160	10	1.04E+13	3.83E+11	1.07E+13
450	linear	1	180	10	1.05E+13	4.29E+11	1.10E+13
451	linear	1	200	10	1.07E+13	4.86E+11	1.12E+13
452	linear	2	0	10	1.64E+13	0.00E+00	1.64E+13
453	linear	2	20	10	1.69E+13	6.68E+10	1.70E+13
454	linear	2	40	10	1.75E+13	1.80E+11	1.76E+13
455	linear	2	60	10	1.80E+13	2.73E+11	1.82E+13
456	linear	2	80	10	1.84E+13	3.67E+11	1.88E+13
457	linear	2	100	10	1.89E+13	4.70E+11	1.94E+13
458	linear	2	120	10	1.94E+13	5.63E+11	1.99E+13
459	linear	2	140	10	1.98E+13	6.42E+11	2.04E+13
460	linear	2	160	10	2.01E+13	7.19E+11	2.08E+13
461	linear	2	180	10	2.04E+13	8.07E+11	2.12E+13
462	linear	2	200	10	2.07E+13	8.93E+11	2.16E+13
463	linear	3	0	10	2.39E+13	0.00E+00	2.39E+13
464	linear	3	20	10	2.48E+13	9.91E+10	2.49E+13
465	linear	3	40	10	2.55E+13	2.69E+11	2.58E+13
466	linear	3	60	10	2.63E+13	4.08E+11	2.67E+13
467	linear	3	80	10	2.68E+13	5.52E+11	2.74E+13
468	linear	3	100	10	2.75E+13	7.06E+11	2.82E+13
469	linear	3	120	10	2.82E+13	8.36E+11	2.90E+13
470	linear	3	140	10	2.88E+13	9.51E+11	2.97E+13
471	linear	3	160	10	2.92E+13	1.06E+12	3.03E+13
472	linear	3	180	10	2.96E+13	1.18E+12	3.08E+13
473	linear	3	200	10	2.99E+13	1.30E+12	3.12E+13
474	linear	4	0	10	3.03E+13	0.00E+00	3.03E+13
475	linear	4	20	10	3.14E+13	1.25E+11	3.15E+13
476	linear	4	40	10	3.22E+13	3.53E+11	3.26E+13
477	linear	4	60	10	3.30E+13	5.31E+11	3.36E+13
478	linear	4	80	10	3.37E+13	7.19E+11	3.44E+13
479	linear	4	100	10	3.44E+13	9.11E+11	3.53E+13
480	linear	4	120	10	3.50E+13	1.07E+12	3.61E+13
481	linear	4	140	10	3.55E+13	1.19E+12	3.67E+13
482	linear	4	160	10	3.59E+13	1.34E+12	3.72E+13
483	linear	4	180	10	3.61E+13	1.49E+12	3.75E+13
484	linear	4	200	10	3.63E+13	1.62E+12	3.79E+13

485	linear	5	0	10	3.47E+13	0.00E+00	3.47E+13
486	linear	5	20	10	3.60E+13	1.46E+11	3.61E+13
487	linear	5	40	10	3.70E+13	4.29E+11	3.74E+13
488	linear	5	60	10	3.78E+13	6.41E+11	3.85E+13
489	linear	5	80	10	3.85E+13	8.60E+11	3.94E+13
490	linear	5	100	10	3.93E+13	1.08E+12	4.04E+13
491	linear	5	120	10	3.99E+13	1.27E+12	4.11E+13
492	linear	5	140	10	4.03E+13	1.41E+12	4.17E+13
493	linear	5	160	10	4.07E+13	1.57E+12	4.23E+13
494	linear	5	180	10	4.08E+13	1.74E+12	4.26E+13
495	linear	5	200	10	4.09E+13	1.89E+12	4.28E+13
496	linear	6	0	10	3.79E+13	0.00E+00	3.79E+13
497	linear	6	20	10	3.95E+13	1.61E+11	3.96E+13
498	linear	6	40	10	4.06E+13	5.05E+11	4.11E+13
499	linear	6	60	10	4.15E+13	7.48E+11	4.22E+13
500	linear	6	80	10	4.24E+13	9.83E+11	4.34E+13
501	linear	6	100	10	4.31E+13	1.23E+12	4.43E+13
502	linear	6	120	10	4.37E+13	1.43E+12	4.52E+13
503	linear	6	140	10	4.42E+13	1.62E+12	4.58E+13
504	linear	6	160	10	4.47E+13	1.79E+12	4.65E+13
505	linear	6	180	10	4.47E+13	1.98E+12	4.67E+13
506	linear	6	200	10	4.48E+13	2.16E+12	4.70E+13
507	linear	7	0	10	4.08E+13	0.00E+00	4.08E+13
508	linear	7	20	10	4.26E+13	1.73E+11	4.28E+13
509	linear	7	40	10	4.39E+13	5.83E+11	4.45E+13
510	linear	7	60	10	4.50E+13	8.55E+11	4.58E+13
511	linear	7	80	10	4.60E+13	1.12E+12	4.71E+13
512	linear	7	100	10	4.67E+13	1.39E+12	4.80E+13
513	linear	7	120	10	4.71E+13	1.61E+12	4.87E+13
514	linear	7	140	10	4.78E+13	1.82E+12	4.96E+13
515	linear	7	160	10	4.82E+13	2.01E+12	5.02E+13
516	linear	7	180	10	4.87E+13	2.24E+12	5.09E+13
517	linear	7	200	10	4.88E+13	2.43E+12	5.12E+13
518	linear	8	0	10	4.36E+13	0.00E+00	4.36E+13
519	linear	8	20	10	4.57E+13	1.83E+11	4.59E+13
520	linear	8	40	10	4.73E+13	6.65E+11	4.79E+13
521	linear	8	60	10	4.85E+13	9.56E+11	4.94E+13
522	linear	8	80	10	4.94E+13	1.25E+12	5.07E+13
523	linear	8	100	10	5.04E+13	1.55E+12	5.20E+13
524	linear	8	120	10	5.11E+13	1.80E+12	5.29E+13
525	linear	8	140	10	5.18E+13	2.03E+12	5.38E+13

526	linear	8	160	10	5.23E+13	2.25E+12	5.46E+13
527	linear	8	180	10	5.19E+13	2.51E+12	5.44E+13
528	linear	8	200	10	5.17E+13	2.68E+12	5.44E+13
529	linear	9	0	10	4.65E+13	0.00E+00	4.65E+13
530	linear	9	20	10	4.89E+13	1.92E+11	4.91E+13
531	linear	9	40	10	5.04E+13	7.47E+11	5.12E+13
532	linear	9	60	10	5.18E+13	1.08E+12	5.29E+13
533	linear	9	80	10	5.28E+13	1.39E+12	5.42E+13
534	linear	9	100	10	5.34E+13	1.72E+12	5.51E+13
535	linear	9	120	10	5.40E+13	1.99E+12	5.60E+13
536	linear	9	140	10	5.49E+13	2.25E+12	5.72E+13
537	linear	9	160	10	5.61E+13	2.49E+12	5.86E+13
538	linear	9	180	10	5.60E+13	2.76E+12	5.87E+13
539	linear	9	200	10	5.63E+13	2.96E+12	5.93E+13
540	linear	10	0	10	4.95E+13	0.00E+00	4.95E+13
541	linear	10	20	10	5.20E+13	1.96E+11	5.22E+13
542	linear	10	40	10	5.41E+13	8.42E+11	5.49E+13
543	linear	10	60	10	5.16E+13	1.08E+12	5.27E+13
544	linear	10	80	10	5.67E+13	1.53E+12	5.82E+13
545	linear	10	100	10	5.78E+13	1.88E+12	5.97E+13
546	linear	10	120	10	5.86E+13	2.16E+12	6.08E+13
547	linear	10	140	10	5.92E+13	2.46E+12	6.16E+13
548	linear	10	160	10	5.24E+13	2.46E+12	5.48E+13
549	linear	10	180	10	5.99E+13	3.03E+12	6.29E+13
550	linear	10	200	10	5.29E+13	2.84E+12	5.57E+13
551	power-law	1	0	10	1.54E+12	0.00E+00	1.54E+12
552	power-law	1	20	10	1.62E+12	6.24E+09	1.62E+12
553	power-law	1	40	10	1.70E+12	2.52E+10	1.73E+12
554	power-law	1	60	10	1.80E+12	5.49E+10	1.85E+12
555	power-law	1	80	10	1.90E+12	9.01E+10	1.99E+12
556	power-law	1	100	10	2.00E+12	1.15E+11	2.12E+12
557	power-law	1	120	10	2.12E+12	1.27E+11	2.25E+12
558	power-law	1	140	10	2.24E+12	1.45E+11	2.39E+12
559	power-law	1	160	10	2.38E+12	1.64E+11	2.54E+12
560	power-law	1	180	10	2.52E+12	1.84E+11	2.70E+12
561	power-law	1	200	10	2.68E+12	2.10E+11	2.89E+12
562	power-law	2	0	10	1.97E+12	0.00E+00	1.97E+12
563	power-law	2	20	10	2.07E+12	7.68E+09	2.08E+12
564	power-law	2	40	10	2.19E+12	2.96E+10	2.22E+12
565	power-law	2	60	10	2.32E+12	6.30E+10	2.38E+12
566	power-law	2	80	10	2.45E+12	1.02E+11	2.55E+12

567	power-law	2	100	10	2.59E+12	1.31E+11	2.72E+12
568	power-law	2	120	10	2.75E+12	1.49E+11	2.90E+12
569	power-law	2	140	10	2.92E+12	1.72E+11	3.10E+12
570	power-law	2	160	10	3.10E+12	1.97E+11	3.30E+12
571	power-law	2	180	10	3.30E+12	2.26E+11	3.53E+12
572	power-law	2	200	10	3.53E+12	2.59E+11	3.79E+12
573	power-law	3	0	10	2.25E+12	0.00E+00	2.25E+12
574	power-law	3	20	10	2.38E+12	8.64E+09	2.39E+12
575	power-law	3	40	10	2.52E+12	3.26E+10	2.55E+12
576	power-law	3	60	10	2.66E+12	6.82E+10	2.73E+12
577	power-law	3	80	10	2.81E+12	1.10E+11	2.92E+12
578	power-law	3	100	10	2.99E+12	1.41E+11	3.13E+12
579	power-law	3	120	10	3.17E+12	1.63E+11	3.33E+12
580	power-law	3	140	10	3.37E+12	1.90E+11	3.56E+12
581	power-law	3	160	10	3.58E+12	2.19E+11	3.80E+12
582	power-law	3	180	10	3.82E+12	2.51E+11	4.07E+12
583	power-law	3	200	10	4.08E+12	2.89E+11	4.37E+12
584	power-law	4	0	10	2.47E+12	0.00E+00	2.47E+12
585	power-law	4	20	10	2.61E+12	9.39E+09	2.62E+12
586	power-law	4	40	10	2.77E+12	3.49E+10	2.80E+12
587	power-law	4	60	10	2.92E+12	7.22E+10	3.00E+12
588	power-law	4	80	10	3.09E+12	1.16E+11	3.21E+12
589	power-law	4	100	10	3.29E+12	1.48E+11	3.44E+12
590	power-law	4	120	10	3.49E+12	1.74E+11	3.67E+12
591	power-law	4	140	10	3.71E+12	2.03E+11	3.91E+12
592	power-law	4	160	10	3.95E+12	2.34E+11	4.18E+12
593	power-law	4	180	10	4.21E+12	2.70E+11	4.48E+12
594	power-law	4	200	10	4.49E+12	3.12E+11	4.81E+12
595	power-law	5	0	10	2.65E+12	0.00E+00	2.65E+12
596	power-law	5	20	10	2.80E+12	1.00E+10	2.81E+12
597	power-law	5	40	10	2.97E+12	3.68E+10	3.01E+12
598	power-law	5	60	10	3.14E+12	7.55E+10	3.22E+12
599	power-law	5	80	10	3.33E+12	1.20E+11	3.45E+12
600	power-law	5	100	10	3.54E+12	1.54E+11	3.69E+12
601	power-law	5	120	10	3.75E+12	1.82E+11	3.93E+12
602	power-law	5	140	10	3.99E+12	2.13E+11	4.20E+12
603	power-law	5	160	10	4.24E+12	2.47E+11	4.49E+12
604	power-law	5	180	10	4.52E+12	2.85E+11	4.81E+12
605	power-law	5	200	10	4.83E+12	3.29E+11	5.16E+12
606	power-law	6	0	10	2.81E+12	0.00E+00	2.81E+12
607	power-law	6	20	10	2.97E+12	1.06E+10	2.98E+12

608	power-law	6	40	10	3.15E+12	3.84E+10	3.19E+12
609	power-law	6	60	10	3.33E+12	7.83E+10	3.41E+12
610	power-law	6	80	10	3.53E+12	1.24E+11	3.65E+12
611	power-law	6	100	10	3.75E+12	1.59E+11	3.91E+12
612	power-law	6	120	10	3.98E+12	1.89E+11	4.17E+12
613	power-law	6	140	10	4.23E+12	2.21E+11	4.45E+12
614	power-law	6	160	10	4.50E+12	2.57E+11	4.76E+12
615	power-law	6	180	10	4.80E+12	2.98E+11	5.09E+12
616	power-law	6	200	10	5.13E+12	3.45E+11	5.48E+12
617	power-law	7	0	10	2.94E+12	0.00E+00	2.94E+12
618	power-law	7	20	10	3.12E+12	1.10E+10	3.13E+12
619	power-law	7	40	10	3.30E+12	3.98E+10	3.34E+12
620	power-law	7	60	10	3.50E+12	8.06E+10	3.58E+12
621	power-law	7	80	10	3.70E+12	1.28E+11	3.83E+12
622	power-law	7	100	10	3.93E+12	1.64E+11	4.10E+12
623	power-law	7	120	10	4.18E+12	1.95E+11	4.37E+12
624	power-law	7	140	10	4.44E+12	2.29E+11	4.67E+12
625	power-law	7	160	10	4.73E+12	2.67E+11	4.99E+12
626	power-law	7	180	10	5.04E+12	3.09E+11	5.35E+12
627	power-law	7	200	10	5.39E+12	3.58E+11	5.75E+12
628	power-law	8	0	10	3.07E+12	0.00E+00	3.07E+12
629	power-law	8	20	10	3.25E+12	1.14E+10	3.26E+12
630	power-law	8	40	10	3.44E+12	4.10E+10	3.48E+12
631	power-law	8	60	10	3.64E+12	8.27E+10	3.72E+12
632	power-law	8	80	10	3.86E+12	1.30E+11	3.99E+12
633	power-law	8	100	10	4.10E+12	1.68E+11	4.27E+12
634	power-law	8	120	10	4.35E+12	2.00E+11	4.55E+12
635	power-law	8	140	10	4.62E+12	2.35E+11	4.86E+12
636	power-law	8	160	10	4.92E+12	2.75E+11	5.20E+12
637	power-law	8	180	10	5.25E+12	3.18E+11	5.56E+12
638	power-law	8	200	10	5.61E+12	3.68E+11	5.98E+12
639	power-law	9	0	10	3.18E+12	0.00E+00	3.18E+12
640	power-law	9	20	10	3.38E+12	1.16E+10	3.39E+12
641	power-law	9	40	10	3.57E+12	4.21E+10	3.61E+12
642	power-law	9	60	10	3.78E+12	8.45E+10	3.86E+12
643	power-law	9	80	10	4.01E+12	1.32E+11	4.14E+12
644	power-law	9	100	10	4.25E+12	1.71E+11	4.42E+12
645	power-law	9	120	10	4.51E+12	2.05E+11	4.71E+12
646	power-law	9	140	10	4.79E+12	2.42E+11	5.03E+12
647	power-law	9	160	10	5.11E+12	2.81E+11	5.39E+12
648	power-law	9	180	10	5.45E+12	3.26E+11	5.77E+12

649	power-law	9	200	10	5.82E+12	3.78E+11	6.20E+12
650	power-law	10	0	10	3.28E+12	0.00E+00	3.28E+12
651	power-law	10	20	10	3.49E+12	1.19E+10	3.50E+12
652	power-law	10	40	10	3.69E+12	4.31E+10	3.73E+12
653	power-law	10	60	10	3.90E+12	8.62E+10	3.99E+12
654	power-law	10	80	10	4.14E+12	1.35E+11	4.28E+12
655	power-law	10	100	10	4.39E+12	1.74E+11	4.57E+12
656	power-law	10	120	10	4.66E+12	2.09E+11	4.87E+12
657	power-law	10	140	10	4.96E+12	2.47E+11	5.20E+12
658	power-law	10	160	10	5.28E+12	2.87E+11	5.57E+12
659	power-law	10	180	10	5.64E+12	3.33E+11	5.97E+12
660	power-law	10	200	10	6.02E+12	3.87E+11	6.40E+12